Ceramics International 52 (2026) 19392–19407

Contents lists available at ScienceDirect

Ceramics International

journal homepage: www.elsevier.com/locate/ceramint

Effect of alkali-activation pre-treatment of sintered aggregates from biomass fly ash on microstructural and mineralogical evolution

Anže Tesovnik [a,b], Vilma Ducman [a,*]

[a] Laboratory for Cements, Mortars and Ceramics, Slovenian National Building and Civil Engineering Institute, Dimičeva ulica 12, 1000, Ljubljana, Slovenia
[b] Jožef Stefan International Postgraduate School, Jamova cesta 39, 1000, Ljubljana, Slovenia

ARTICLE INFO

Keywords:
Alkali-activated materials
Biomass ash
Sintered artificial aggregates
Lightweight construction materials

ABSTRACT

The increasing demand for lightweight construction materials and the depletion of natural aggregates highlight the need for circular solutions based on industrial residues. Co-incineration biomass ash (BA), despite its high availability, carbon content, and variable composition, remains underutilised in high-value applications. This study explores a previously unexamined valorisation route through the production of sintered alkali-activated aggregates using sodium-silicate-assisted pre-treatment. Two BA mixes with different Na_2O dosages (7.57 and 5.44 wt% Na_2O) were pelletized and thermally treated between 700 and 1200 °C. The alkali activation pre-treatment simultaneously improved the granulation efficiency, enabled the formation of alkali-activated gel, and supplied Na_2O as a flux, significantly influencing the crystalization, melting, and sintering behavior. Comprehensive characterisation using mercury intrusion porosimetry, dilatometry, X-ray diffraction, Fourier-transform infrared spectroscopy, thermogravimetry–differential thermal analysis, and scanning electron microscopy revealed a coherent thermal sequence: from gel deterioration and a macroporosity development below 800 °C, to the crystallization of Ca–Mg silicates and the formation of an akermanite-dominated matrix at 800–1000 °C, followed by partial melting and sintering in the presence of a liquid phase above 1000 °C. A higher alkali content promoted earlier densification and strength development. Aggregates with higher Na_2O content (BA1) exhibited an earlier onset and higher intensity of sintering shrinkage, reaching a compressive strength of 4.53 MPa at 1100 °C, corresponding to more than a fourfold increase compared to thermally untreated aggregates, whereas the lower-alkali mix (BA2) remained below 0.26 MPa at the same temperature. Open porosity of BA1 aggregates increased to 78.8% after heating to 800 °C due to deterioration of the alkali-activated gel, followed by densification accompanied by akermanite-dominated crystallization and pore coalescence, resulting in 73.1% porosity and a bulk density of 1.28 g/cm^3 at 1100 °C. The results identify BA as a promising precursor for lightweight or dense SAA and demonstrate alkali-activation-assisted thermal treatment to be a technically applicable circular-economy pathway for converting co-incineration BA into value-added construction materials.

1. Introduction

Excavating natural aggregates causes the destruction of natural topography and leads to an overexploitation of raw materials, with some countries already introducing restriction policies to mitigate resource scarcity. In contrast to unsustainable raw material exploitation, the growing problem of industrial by-products and waste disposal is forcing industries to consider recycling and reuse within a circular approach. At the European regional level, the Waste Framework Directive [1] introduces the general concept of EU waste policy by defining the waste hierarchy, emphasizing reuse, recycling, and recovery. Additionally, product regulations, such as the recently revised EU Construction Products Regulation [2], require compliance with sustainability and environmental performance standards. These regulations encourage environmental declarations and life cycle assessments. Their circular economy requirements, such as recycled content and easier reuse, are being updated. The European Green Deal initiative, with its Circular Economy Action Plan [3], targets resource-intensive sectors, especially construction and building materials, setting norms for sustainable products that follow closed material loops. National level implementations often include additional landfill taxes, recycling incentives, carbon pricing through emissions trading systems, and higher taxation on virgin raw materials. This increases the pressure on industry to seek new

* Corresponding author.
E-mail address: vilma.ducman@zag.si (V. Ducman).

https://doi.org/10.1016/j.ceramint.2026.03.041
Received 27 November 2025; Received in revised form 26 February 2026; Accepted 4 March 2026
Available online 4 March 2026

Abbreviations

AAM	Alkali-activated materials
BA	Co-incineration biomass ash
DTA	Differential Thermal Analysis
EDXS	Energy-Dispersive X-ray Spectroscopy
FTIR	Fourier-Transform Infrared Spectroscopy
MIP	Mercury Intrusion Porosimetry
SAA	Sintered Alkali-activated Aggregates
SEM	Scanning Electron Microscopy
TG	Thermogravimetric Analysis
XRD	X-ray Diffraction
XRF	X-ray Fluorescence

strategies that are sustainable as well as economically viable. One promising pathway to comply with these environmental ambitions is the valorisation of waste materials through their transformation into artificial aggregates.

Considering that aggregates constitute up to 70% of a concrete volume [4], the valorisation of waste into artificial aggregates offers a more effective and volumetrically impactful utilization pathway than conventional practices such as using waste as partial cement [5] or concrete replacements [6,7]. The reuse of ashes in construction materials is governed by several standards (EN 197–1 for cement, EN 450–1 and ASTM C618 for concrete), which impose strict compositional and performance requirements that often limit the use of biomass ashes in conventional cementitious (Ordinary Portland cement) systems due to their high carbon and organic content. In this context, aggregate production offers an alternative valorisation pathway, enabling high-volume utilization of biomass ashes in value-added construction products. Such artificial aggregates can be produced using alternative binders through alkali activation, in which a chemical process between the reactive amorphous silica and alumina, present in various industrial residues, and an alkaline solution forms a stable solid alkali-activated material [8,9]. This approach not only replaces natural aggregates in specific applications, but also enables the design of materials with a low density [10,11], controlled porosity [12], high chemical resistance [13], good insulating capacity, acoustic absorption [14], and thermal stability [15], while maintaining compressive strengths comparable to natural lightweight aggregates such as expanded clay or perlite.

The most common methods of producing artificial aggregates are sintering and cold-bound pelletization [16]. Traditional sintered aggregates are initially formed by pelletization using either disc or drum pelletizers in which powders are mixed with a small amount of water [17]. Sometimes clays such as bentonite are added to improve the particle adhesion and granule shape retention [18,19]. Moist particles adhere through surface tension and capillary forces, forming rounded granules during rotation. The fresh, unsintered granules are then dried to remove moisture and sintered in a furnace or rotary kiln, where partial melting at high temperatures fuses the particles internally [18]. Research on sintered aggregates and their commercial production began relatively early, with the first reports of sintered coal fly ash (FA) aggregates appearing in the 1960s [20]. To lower the high sintering temperatures, which in the case of FA can exceed 1100 °C, fluxing agents are commonly used to reduce the melting point and make the process less energy-intensive. Traditional sintered aggregates are typically produced by combining (non-waste) FA with CaO or Fe_2O_3 as fluxing and binding agents [21], or by incorporating waste clays, sludges, and glass waste (Na_2O–SiO_2 sources) [22]. In contrast, cold-bonding manufacturing uses a small amount of binder to form granules at temperatures below 100 °C. Conventional cold-bonded aggregates typically use ordinary Portland cement (OPC) in amounts up to 20 wt% as a binder for waste materials [23,24], which can also serve for waste stabilization. However, waste materials with low reactive Ca content often result in weak or unreacted inclusions and poor binding. Moreover, reactive oxides, as well as elevated sulfate and chloride contents, can interfere with cement hydration or induce delayed ettringite or thaumasite formation [25], leading to cracking, expansion, and long-term instability. Furthermore, using OPC, which is responsible for 0.8–0.9 tons of CO_2 per ton of cement, undermines the sustainability benefit of recycling wastes. On the other hand, alkali-activated cold-bonded aggregates, proposed in the late 2010s [26], are emerging as a more sustainable alternative for aggregating waste containing reactive amorphous aluminosilicate phases (various ashes, agricultural ashes, unconventional slags, clays, and sediments). These material precursors are bound by the addition of alkaline solution, most commonly sodium silicate and sodium hydroxide [8], to form granules based on alkali-activated materials (AAM).

Besides traditional sintering and cold-bonded alkali-activated aggregation, the field of sintered alkali-activated aggregates (SAA) is relatively new, with a limited number of studies investigating the combination of sintering and alkali activation in the production of artificial aggregates. In this process, aggregates are first alkali-activated by adding a high-pH activating solution. The fresh granules consist of newly formed reacted alkali-activated phases, such as C–A–S–H, N(C)–A–S–H, or N–A–S–H gels [27–29], together with unreacted particles that act as inert fillers. The shaped alkali-activated granules are subsequently subjected to thermal treatment for sintering. Such pre-treatment through alkali activation alters the initial chemical and phase composition, which can modify the sintering mechanisms compared to conventional sintering. Furthermore, our previous study demonstrated that the addition of an alkaline silicate solution enhances the granulation efficiency compared to water-only control samples [12]. This improvement reduces the amount of unbound waste residue generated during granule formation in a disc pelletizer and thus increases the economic efficiency of the pre-sintering shaping process for waste-derived materials.

Only a limited number of studies have investigated the sintering of alkali-activated material aggregates, with the earliest reports appearing around 2013 [30]. Most studies focused on valorizing coal FA through alkali activation combined with thermal sintering, but their experimental scopes were narrow and often lacked a systematic evaluation of process parameters. Razak et al. [31] studied alkali-activated volcanic ash granules, first cured at 60 °C and then sintered at 500, 600, and 800 °C for 1 h. The granules were handshaped in the fresh state after mixing with sodium silicate, limiting the industrial relevance of the findings. The thermal treatment was applied in coarse temperature steps of 200 °C and limited to relatively low maximum temperatures. The evaluation focused on physical–mechanical properties relevant to construction applications of artificial aggregates such as water absorption, specific gravity, and apparent porosity, without employing chemical or mineralogical analyses. Similarly, Abdullah et al. [32] produced alkali-activated coal FA aggregates cured at 70 °C for 24 h and then thermally treated between 500 °C and 700 °C, a narrow and moderate temperature range that provides limited insight into the full thermal evolution of the material. Increased strength and reduced open porosity were observed, but sintering was conducted only on a single mix composition with the highest initial compressive strength after pre-sintering alkali activation. Terzić et al. [33] manufactured cold-bonded FA aggregates with sodium silicate, cured at 20 °C and 70% relative humidity, and later sintered at 1100 and 1200 °C. Compared to earlier studies, this work employed substantially higher sintering temperatures and included a more comprehensive characterization of the sintered aggregates. Razak et al. [34] hand-shaped volcanic mud aggregates, activated with sodium silicate and NaOH, cured at 60 °C for 5 h, and sintered at 950 °C for 1 h. Gomathi and Sivakumar [35] prepared coal fly ash–bentonite–OPC aggregates, reporting that the addition of NaOH improved their stability before sintering at 950 °C for 1 h. Abdullah et al. [36] also sintered hand-shaped high-calcium FA aggregates, activated with sodium hydroxide and sodium silicate, curing one

mix design at 70 °C for 24 h and sintering up to 900 °C, focusing mainly on their use in concrete. Lau et al. [21] used a disc pelletizer to form aggregates from lime-treated sewage sludge, palm oil fuel ash, and sodium silicate, which were sintered at 1160–1200 °C. It was reported that a higher binder content and temperature improved the compressive strength. Risdanareni et al. [37] used a pan pelletizer to granulate coal FA with sodium silicate and NaOH, cured at 100 °C for 24 h, and sintered at 900 °C for 6 h. The performance of the sintered coarse aggregates was evaluated in embedded concrete specimens, where full replacement of natural coarse aggregates with sintered aggregates resulted in compressive strengths of up to approximately 32 MPa. Recent studies have explored the chemical activation of non-granulated foamed materials prior to thermal processing. Hujová et al. produced glass-ceramic foams from vitrified bottom ash and waste glasses using weak alkaline activation followed by foaming and crystallization. They demonstrated that gel formation at low alkalinity can enable pore development and stabilization of recycled materials [38].

Despite these efforts, several drawbacks are evident in the currently published research on SAA. Most studies used only one mix composition, limiting the comparability and optimisation potential. It is important to note that coal fly ash, the most commonly used precursor for SAA in previous studies and once considered a waste, has become a valuable secondary raw material, widely used as a cement replacement due to its pozzolanic reactivity. In contrast, other waste materials such as biomass FA remain underutilised in cementitious applications, despite having suitable chemistry for binding through alkali activation. Moreover, the potential role of high residual carbon in biomass ashes during alkali activation and subsequent thermal treatment, particularly its influence on pore formation and the desired lightweight microstructure of aggregates, has not been systematically explored. The sintering temperature range in the literature was often narrow and inadequately explored, which may result in missing the optimal temperature for achieving desired aggregate properties, overlooking the optimal sintering window, and limiting understanding of material evolution under thermal treatment. Hand-shaped aggregates were commonly used instead of mechanically pelletized granules, reducing the representativeness of manually shaped aggregates and relevance of the results to industrial-scale manufacturing. The previously reported results primarily focused on the final mechanical or physical properties relevant to construction lightweight aggregates (e.g., compressive strength, water absorption, inclusion in concrete), while providing limited insight into thermal treatment behavior, sintering mechanisms, phase evolution or microstructural development during gradually increasing thermal treatment. Furthermore, none of the studies systematically investigated the influence of pre-sintering alkali activation and sodium silicate dosage on the thermal evolution, phase transformations, and densification behavior of SAA. In the present study, waste co-incinerating biomass ash (BA) characterized by a high carbon (unburnt wood particles), SiO_2, Al_2O_3 and CaO contents, was used as the primary precursor for alkali-activated aggregates. A sodium silicate solution served as both a binder, enhancing pelletization efficiency and chemical activation, and a fluxing agent, reducing the sintering temperature. The previously unexamined effects of alkali dosage and fluxing on the thermal behavior of lightweigh aggregates were systematically investigated from micro-to macrostructural levels in two mixtures with different amounts of sodium silicate. The lightweight aggregates were produced using industrially accepted mechanically controlled rotational disc pelletization and subjected to thermal treatment over a broad temperature range from 700 °C to 1200 °C. The effects of temperature and pre-sintering alkali-activation were evaluated by mechanical performance, porosity, dimensional stability, thermal behavior, mineralogical and phase evolution, and microstructural development.

2. Materials and methods

2.1. Raw materials and aggregate preparation

Ash from the co-incineration of brown coal and wood waste from a local Slovenian thermal power plant was used as a solid precursor to produce artificial lightweight aggregates. The chemical composition of the co-incineration biomass ash (BA) used in the study was analyzed using X-ray fluorescence spectroscopy (XRF; Thermo Scientific ARL Perform'X Sequential XRF spectrometer) on molten discs, as presented in Table 1. The loss on ignition (LOI) of dried samples to constant mass (50 °C, 24 h) was determined by heating to 550 °C and 950 °C for 2 h. The BA is characterised by a high content of Si and Al, which are recognised as key network formers for alkali-activated binding systems. Previous studies have demonstrated that a significant fraction of Si and Al in BA is present in an amorphous or poorly crystalline phase [12], making it chemically reactive under alkaline conditions and suitable for alkali activation.

The BA exhibits the following particle size distribution parameters: d10, d50 and d90, corresponding to 7.8, 50.2, and 299.1 μm, respectively. The measurments were determined using a Microtrac MRB Sync + TurboSync laser diffraction granulometry analyzer on samples suspended in an isopropanol dispersion bath with ultrasonication. The graph of the differential and cumulative particle size distribution of BA is presented in Fig. 1a. The BA has a high organic content, as confirmed by loss on ignition (LOI) measurements, which reached 14.3% at 550 °C and 16.9% at 950 °C, indicating a significant presence of unburned organic matter. The SEM micrograph in Fig. 1b and the EDXS analysis in the Supplementary data (Fig. S1 and Table S1) confirm the presence of incompletely combusted cellulose particles from wood biomass, which mostly represent a secondary peak in the differential particle size distribution.

X-ray diffraction (XRD) was performed using an Empyrean PANalytical X-ray diffractometer (Cu X-ray source, 45 kV, 40 mA) on the BA precursor ground to below 90 μm to characterize the crystalline fraction of BA. The pattern was evaluated by Rietveld refinement using the X'Pert HighScore Plus software v. 4.8. XRD analysis was performed between 4° and 70° with a step size of 0.0263°. In the BA precursor, the main dominant crystalline phases are quartz and calcite, while the amorphous phase represents more than 45 wt% (Fig. 2).

Lightweight alkali-activated aggregates were prepared by mixing the BA precursor with a sodium silicate solution (Geosil 34417, Wöllner; chemical composition: SiO_2 27.5 m%, Na_2O 16.9 m%, H_2O 55.6 m%) and tap water. The mix design was adapted from a previous study on alkali-activated BA-based aggregates [12] and developed following compositional principles established for alkali-activated materials by Duxson et al. [39], where a Si/Al molar ratio close to 1.9 was shown to promote optimal mechanical performance of AAM through enhanced aluminosilicate gel formation. Since BA can exhibit considerable compositional variability depending on fuel origin and combustion conditions, the direct applicability of the proposed mix design and processing aggregation requires precise mix design considering chemical composition. Two formulations were produced to represent different degrees of alkali activation: one with a higher proportion of alkaline solution (BA1, corresponding to a Si/Al molar ratio of 1.9) and one with a lower proportion of alkaline solution (BA2, corresponding to a Si/Al molar ratio of 1.6) to evaluate the influence of solid alkali on thermal treatment. Additional water was added to achieve a w/s ratio of 0.5, which, based on previous tests, allows an adequate application of the solution by spraying. The detailed mix compositions are presented in Table 2 normalized to 100 g of precursor. The targeted compositional variation enabled evaluation of the influence of alkali availability and pre-sintering gel formation on subsequent thermal evolution and sintering behavior.

The artificial aggregates were produced using a rotational disc pelletizer EIRICH TR04. The dry BA precursor was first introduced into a

Table 1
Chemical composition of co-incineration BA used as precursor, according to XRF analysis.

Na_2O	MgO	Al_2O_3	SiO2	P_2O_5	SO_3	K_2O	CaO	Fe_2O_3	TiO_2	$LOI^{550\ °C}$	$LOI^{950\ °C}$
0.39	7.88	10.8	27.19	0.6	1.26	2.12	19.67	11.95	0.53	14.3	16.9

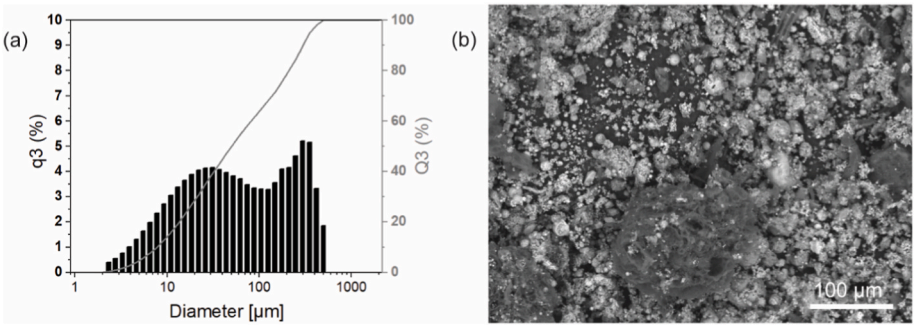

Fig. 1. (a) Differential q_3 and cumulative Q_3 particle size distribution of BA. (b) SEM micrograph of BA at × 250 magnification.

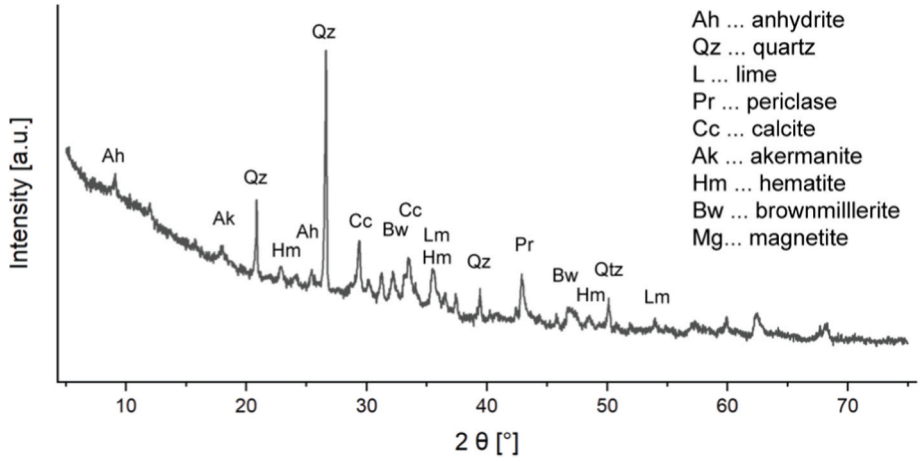

Fig. 2. XRD diffractogram of the BA precursor.

Table 2
Mix design of BA for producing artificial aggregates through alkali activation.

Granulation mix	BA precursor	Na_2SiO_3 activator	Added water	Total solid alkali from Na_2SiO_3
	[g]	[g]	[g]	[g]
BA1	100	44.8	25.2	7.57
BA2	100	32.2	32.2	5.44

40 cm rotating pan, inclined at 45° (Fig. 3). Granulation was carried out following the variable-speed pelletization approach described in Ref. [12], which enables the formation of a highly porous, lightweight structure with a high granulation efficiency, limiting the amount of unbound material remaining after rotational granulation. After granulating the BA, the artificial aggregates were uniformly spread on plastic plates and cured for 7 days under controlled laboratory conditions (20 ± 1 °C, 55 ± 5% relative humidity) to ensure consistent drying and structural stability.

2.2. Thermal treatment of alkali-activated aggregates

On the 8th day after preparation, the alkali-activated BA aggregates were subjected to thermal treatment in a laboratory furnace (Protherm PLF 160/9). Both aggregate mixtures were exposed to target temperatures of 700, 800, 900, 1000, 1100, and 1200 °C (Fig. 4). The heating regime began with an initial stage at a heating rate of 5 °C/min up to 300 °C to allow a gradual removal of physically bound water and minimise internal pressure build-up that could cause cracking, bloating, or bursting. The heating rate was then increased to 10 °C/min until the maximum set temperature was reached. Each target temperature was maintained for 30 min, after which the aggregates were allowed to cool to ambient temperature inside the furnace.

2.3. Characterization methods of thermally treated alkali-activated aggregates

Compressive strength measurements of thermally treated aggregates were performed on 10 coarse aggregates with sizes ranging from 8 to 9 mm. A ToniTechnik ToniNORM mechanical testing machine was used to apply compressive force at a constant loading rate of 0.05 kN/s. The diameter of the spherical aggregates was measured using a digital calliper with an accuracy of ±0.02 mm. The compressive strength (CS) of the aggregates was calculated according to Eq. (1) [40]:

$$CS = (CF * 2.8) / (\pi * d^2) \quad (1)$$

where CF is the maximum compressive force at failure [kN] and d is the diameter of the aggregate (mm). The coefficient 2.8 is a shape correction factor applied for approximation of spherical aggregates.

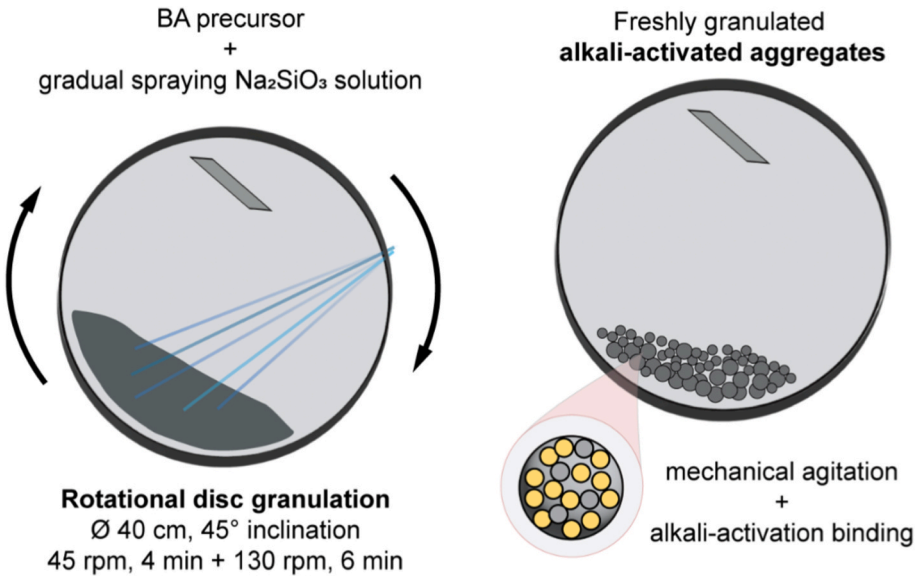

Fig. 3. Schematic presentation of the alkali-activation-assisted granulation process for artificial aggregates, used in this study.

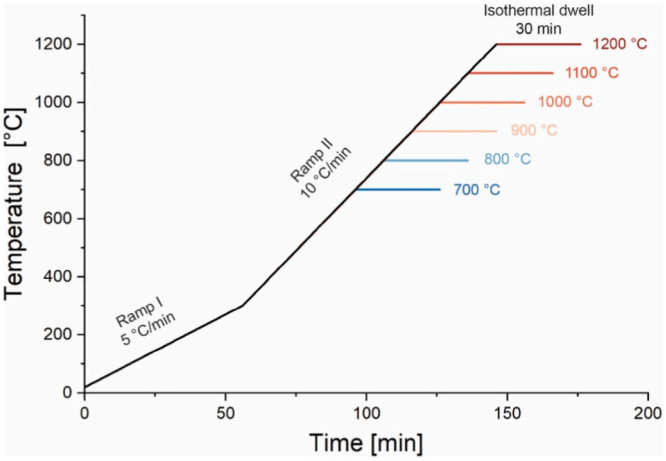

Fig. 4. Heating program applied for thermal treatment of alkali-activated BA aggregates.

Dilatometric analysis was conducted to assess the thermal stability behavior of the alkali-activated BA mixes, using a Netzsch DIL 402 PC dilatometer, with heating up to 1100 °C at a rate of 10 °C/min. Prismatic samples of 8 × 8 × 20 mm were prepared, as required by the push-rod dilatometer configuration, which necessitates samples with parallel, flat surfaces to ensure reliable displacement measurement. In addition to the mix designs described in Table 2, calculated efficiency-normalized mixtures were prepared to account for the influence of the granulation process efficiency and to approximate the composition of aggregates formed under realistic disc pelletization conditions. During granulation in the disc pelletizer, the sprayed alkaline solution promotes the binding of powder particles into granules through liquid-bridge formation and chemical reactions of alkali activation. However, a fraction of BA powder remains unbound due to insufficient liquid for capillary bonding or chemical reaction, which was taken into account in the calculated efficiency-normalized mixtures. Granulation efficiency, defined as the resulting mass fraction of aggregates larger than 4 mm relative to the total batch mass, was considered in the preparation of granulation efficiency-normalized prisms. Based on values from a previous study of BA granulation [12], the BA1 mix was normalized to an efficiency of 78% (adjusting the weight of precursor to 78 g), and the BA2 mix to 75% (adjusting to 75 g of precursor). The amounts of alkaline solution and additional water in the normalized mixes were kept identical to those in the original non-normalized mixtures (Table 2), ensuring a representative approximation of the actual aggregate composition.

Mercury intrusion porosimetry (MIP) was performed on selected thermally treated aggregate samples using a Micromeritics Autopore IV 9500 porosimeter to determine the pore size distribution and total porosity. Intrusion measurements were conducted over a pressure range of 0.5 to 60000 psi, allowing the quantification of open porosity and pore size distribution from the micro-to the macro-scale.

XRD analysis was performed to assess the effect of thermal treatment on the mineralogical composition and amorphous content of the aggregates. The analyses were carried out using an Empyrean PANalytical diffractometer on thermally treated samples that were ground and sieved to below 90 μm. The powdered samples were back-loaded into sample holders and scanned over a 2θ range of 4–70°, with a step size of 0.0263°. Phase identification and quantification were performed by Rietveld refinement using X'Pert HighScore Plus software (version 4.8). The amorphous phase was determined by the external standard method, using NIST SRM 676a (Al_2O_3, corundum) as the internal reference material.

Differential thermal analysis (DTA) and thermogravimetric (TG) measurements were performed to evaluate the thermal decomposition behavior and mass-loss processes of the alkali-activated BA mixes. The analyses were carried out using a NETZSCH STA 409 PC/PG simultaneous thermal analyzer. Powdered samples were placed in an Al_2O_3 crucible, with an empty crucible used as the reference. The measurements were conducted under a nitrogen atmosphere with a 20 mL/min N_2 purge gas flow. The samples were heated from 25 °C to 1050 °C at a constant heating rate of 10 °C/min.

Fourier-transform infrared spectroscopy (FTIR) was performed to identify the chemical bonds and functional groups present in the thermally treated aggregates. The spectra were recorded using a PerkinElmer Spectrum Two spectrometer equipped with an attenuated total reflectance (ATR) accessory featuring a diamond/ZnSe crystal. Measurements were performed in the wavenumber range of 380–4000 cm^{-1}, with a spectral resolution of 4 cm^{-1}.

Scanning electron microscopy (SEM) combined with energy-dispersive X-ray spectroscopy (EDXS) were performed using a JEOL JSM-IT500 to investigate the microstructural changes in the aggregates resulting from thermal treatment.

3. Results and discussion

The effect of thermal treatments (between 700 and 1200 °C) on the size and appearance of AAM aggregates from BA is shown in Fig. 5. Compared to the untreated aggregates, both mixes changed in color from grey to a brownish tone after high temperature exposure. Up to 900 °C, both BA1 and BA2 maintained their spherical shape. At 1000–1100 °C, BA1 aggregates with higher alkali content showed an earlier onset of surface densification and darkening compared to BA2 (lower alkali content). BA1 exhibited a more intense colour change. At the final temperature of 1200 °C both materials became flat, indicating that they partially melted.

3.1. Mechanical properties

The compressive strength of the aggregates exhibited a strong dependence on the thermal treatment temperature (Fig. 6). For the BA1 mix, only a slight increase in strength was observed up to 1000 °C (0.32–0.57 MPa), remaining below the non-treated reference strength of 1.08 MPa [12,41]. This 70% strength reduction with initial heating to 700 °C is consistent with previous studies reporting a thermal degradation of C–A–S–H type alkali-activated matrices at elevated temperatures due to the dehydration of structural water, a collapse of the gel network, and gas evolution within the pore structure. Such thermally induced destabilisation of the aluminosilicate framework has been widely documented in thermal resistance studies of AAMs, where strength losses of 40–80% are typically observed prior to the onset of sintering [40]. However, the extent of thermal degradation in AAM systems strongly depends on the precursor chemistry, type of activator solution, mix design and shape design. High-calcium alkali-activated systems, such as slag- or BA-based AAMs, exhibit a fast reaction degree with alkaline activators and typically do not require prolonged curing [42]. Consequently, they are well suited for granulation processes, where chemical binding can initiate already during mechanical rotational shaping [12]. In contrast, low-calcium geopolymers produced by alkalination of precursors such as FA Class F and metakaolin exhibit slower reaction kinetics and limited early-age strength development, often requiring prolonged curing [43,44]. The primary binding phase in these systems is an N–A–S–H gel, which forms a more stable three-dimensional aluminosilicate network and typically results in improved resistance to elevated temperatures [45]. Traven et al. [46] exposed Na-based blended metakaolin and high-Ca FA prisms foamed with 1 mass % H_2O_2 to thermal treatment and reported a strength drop

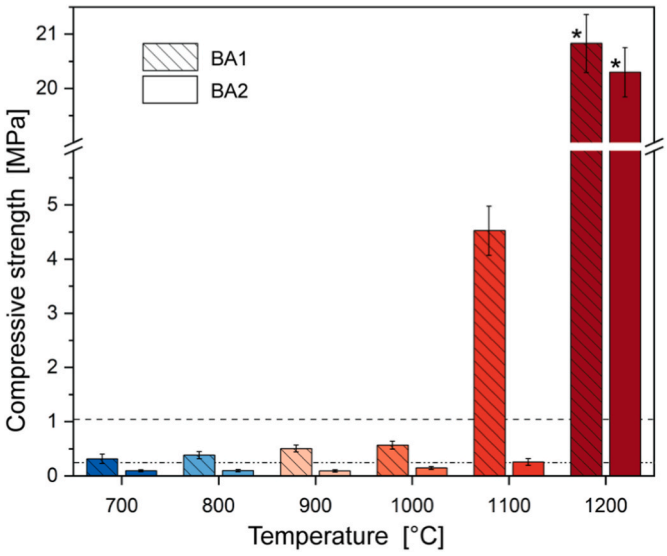

Fig. 6. Compressive strength of BA1 and BA2 aggregates after thermal treatment. Horizontal dashed lines indicate the compressive strengths of the respective untreated aggregates (BA1 = 1.08 MPa and BA2 = 0.24 MPa). Values at 1200 °C (*) are approximate due to shape deformation.

after exposure to 600 °C, with a 45–86% reduction depending on the mix design. The thermal stability of high-Ca FA was lower compared to blends with metakaolin. The strength reduction was also linked to a decrease in bulk density compared to unexposed samples.

A pronounced increase in strength was observed with aggregates treated at 1100 °C, where BA1 reached 4.53 MPa, followed by a further rapid increase to 20.83 MPa at 1200 °C. Compared to the untreated aggregate, this corresponds to a 419% increase after treatment at 1100 °C and a 1929% increase after treatment at 1200 °C, indicating the onset of melting and densification of microstructure, accompanied by a significant reduction in open porosity. However, aggregates treated at 1200 °C underwent a significant shape deformation due to softening and partial melting of both mix designs. Therefore, the assumption of near-spherical geometry (Eq. (1)) is not fully valid for the calculation of strength values at that temperature and likely represents an approximation rather than the absolute mechanical strength, although the strength development trend remains valid according to the literature

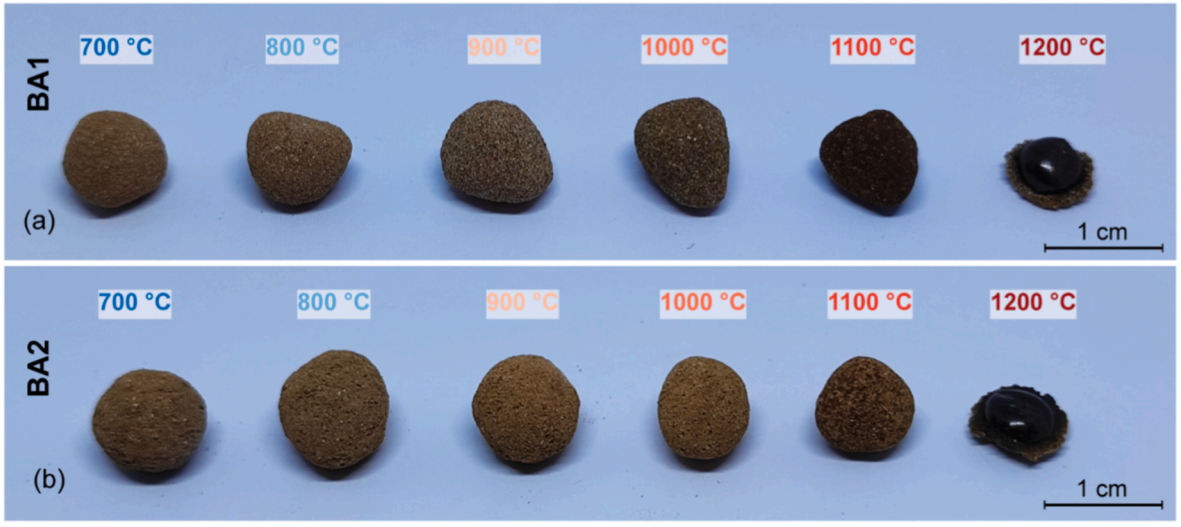

Fig. 5. Aggregate appearance after thermal treatment at different temperatures: (a) Aggregates prepared from the BA1 mix; (b) Aggregates prepared from the BA2 mix.

[46].

In contrast, the BA2 mix exhibited a very limited strength up to 1100 °C (0.09–0.26 MPa), remaining below or near the reference value for the untreated BA2 material (0.24 MPa). The smaller relative reduction in strength observed for BA2 during heating (700–1000 °C) indicates the fact that less alkali-activated binder gel was successfully formed during initial synthesis and curing. A weaker structural alkali-activated framework and lower initial stability of the gel were due to suboptimal activator dosing and a non-ideal Si/Al ratio (1.6 instead of the theoretically optimal 1.9), as reported in a previous study [12]. Consequently, the BA2 matrix had a lower initial load-bearing AAM framework, and therefore had less mechanically effective gel available to degrade upon heating. Limited early polymerization of AAM results in a lower absolute loss of strength during initial thermal exposure. Similarly, Potchara et al. [47] observed that AAM mortars with higher amounts of unreacted particles due to excessive NaOH activator concentrations showed a lower reduction in compressive strength compared to more optimal activator dosing.

Comparing the strength development during increasing temperatures of the treatment between the BA1 and BA2 aggregate series enables to observe a notable difference. BA1, which contains a higher Na_2O content due to an increased dose of sodium silicate solution, shows a markedly faster onset of sintering and earlier strength gain. In contrast, BA2, with a lower alkali input, exhibits a delayed sintering response and correspondingly slower strength development. These findings confirm that alkali availability in SAA aggregates, particularly Na_2O, is a key factor controlling the thermal consolidation of waste-derived aggregates. Similar fluxing effects of sodium have been reported in the literature on ceramics and bricks. Feldthus et al. [48] demonstrated that the addition of sewage sludge ash, due to the presence of Fe and Na, has a fluxing effect on sintering and melting in fired bricks. Likewise, waste glass containing high Na_2O has been shown to reduce sintering temperatures and improve overall processing efficiency [49]. Billen et al. [48] also reported that NaOH addition acted as an effective flux during the melt-based production of coal-ash ceramic aggregates. Certain industrial waste, such as sewage sludge ash, bauxite residue [50], or waste glass wool [51,52], naturally contain sufficient Na_2O to enhance melting and sintering in the presence of liquid phase, and can also be used in alkali-activation due to their high reactivity and sufficient SiO_2 and Al_2O_3 content. Other low Na_2O precursors can benefit from the addition of external sodium-based activators to achieve a comparable thermal behavior. In this study, the incorporation of Na_2SiO_3 solution provided multiple benefits during aggregate production. First, the higher viscosity and density of the alkaline silicate solution (compared to water or alkali hydroxide activators) improve pelletization efficiency on the rotating disc [12], promoting the formation of spherical granules with reduced dusting and a lower fraction of unbound fine residue particles. Second, Na_2SiO_3 served as an additional Na_2O source, facilitating: (i) initial alkali activation and structural stabilization, and (ii) acting as a flux agent that lowered the effective sintering temperature during firing.

However, heating to 1200 °C also increased the compressive strength uppon cooling BA2 to 20.30 MPa, converging with the performance of BA1. This indicates that above the sintering threshold, compositional differences between BA1 and BA2 become less influential, as extensive melting and potential pore closure dominate microstructural evolution.

Although the highest mechanical performance was achieved at 1200 °C, the associated energy demand must be considered when evaluating technical applicability. It should be emphasized that complete melting of the aggregates is not the intended processing objective of waste granulation. Instead, the formation of a lightweight, porous structure is desired, requiring an optimized balance between mechanical strength, porosity, and functional performance according to the targeted application. The pre-treatment alkali-activation process should be considered a hybrid manufacturing approach that combines chemical activation and thermal processing. Unlike conventional AAMs, which often require prolonged low-temperature curing periods lasting hours or days, the present system achieves rapid consolidation through short-duration sintering, where pre-treatment enhances precursor reactivity, increases granulation efficiency, and introduces alkali fluxes that promote earlier strength gain.

3.2. Porosity and density

The open porosity and bulk density of the BA1 aggregates determined by MIP are presented in Table 3, while the corresponding pore size distributions are shown in Fig. 7. The aggregates thermally treated at 700 °C exhibit very high open porosity of 72.3% and a low bulk density of 0.97 g/cm^3. The open porosity system is dominated by a broad population of interconnected macropores (>10 μm), as evidenced by the wide main intrusion peak at 30 μm (Fig. 7). Such a highly interconnected pore network provides limited load-bearing capacity, which is consistent with the observed reduction in compressive strength compared to the untreated aggregates (Fig. 6), where the reported porosity of 45.4% is significantly lower [12].

Upon heating to 800 °C, the bulk density further decreases to 0.90 g/cm^3, accompanied by an increase in total open porosity to 78.8%. This behavior correlates with the emergence and intensification of macroporosity, indicating further thermal degradation of the aluminosilicate gel network and gas evolution within the pore structure. The similar pore forming behavior has been observed in previous studies on thermal evaluation of Ca-rich alkali-activated materials and it was attributed to pore expansion due to microstructural changes in the binding gel [53], dehydroxilation and microcrack propagation [54] and internal strain contribution [55].

With further heating to 900–1000 °C, the bulk density gradually increased while the open porosity slightly decreased. This transition is reflected in the pore size diameter distribution curves by a reduction in the intensity of intrusion peaks associated with smaller macro and mesopores (<5 μm) (Fig. 7). This indicates the onset of microstructural reorganization, initial crystallization and bonding at particle contacts [56,57]. At the same temperature heating range of 900–1000 °C, the reduced height of the intrusion peak indicates partial pore closure, while the main pore diameter peak gradually shifts towards larger pores, indicating pore coalescence (merging of smaller pores into coarser ones) driven by surface energy minimization, consistent with an Ostwald ripening mechanism [58]. Although total porosity remains high, the reduction in fine pores improves local contact areas between solid phases, explaining the modest recovery of strength observed up to 1000 °C (Fig. 6).

A notable transition in porosity occurres in aggregates heated to 1100 °C, where open porosity decreased to 73% and the bulk density increased to 1.28 g/cm^3. The reduced intrusion signal across the entire pore size range indicates decreased porosity and pore accessibility due to partial melting and sintering in the presence of a liquid phase [57,59]. The collapse and sealing of pores slightly reduce the effective open porosity to 73 %, even though residual macropores remain present. The pore coalescence and densification provide a transition from a mechanically weak, porous structure to a consolidated load-bearing structure, which correlates with the first substantial increase in compressive strength (Fig. 6).

After treatement at 1200 °C, total porosity is significantly reduced to

Table 3
Open porosity and bulk particle density of BA1 aggregates after thermal treatment at various temperatures.

T [°C]	Open porosity [%]	Bulk density [g/cm^3]
700	72.27	0.965
800	78.75	0.903
900	77.03	0.917
1000	76.87	0.920
1100	73.09	1.284
1200	34.02	2.817

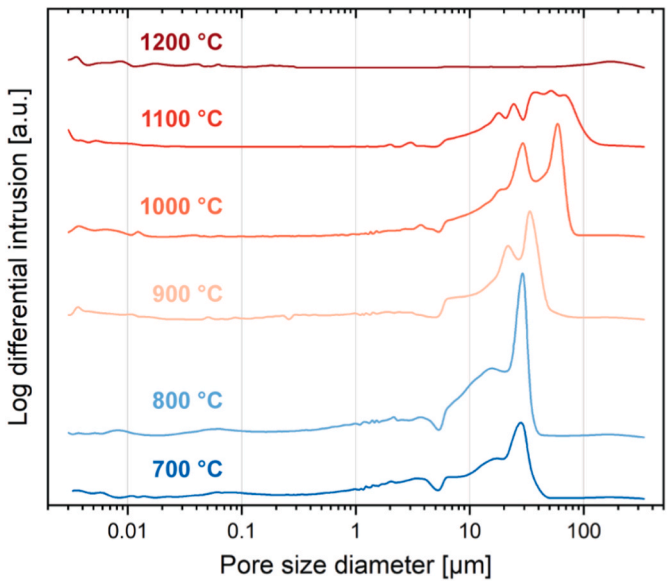

Fig. 7. Pore size distribution of BA1 aggregates.

34%, together with an increase in bulk density to 2.82 g/cm^3. The pore distribution curve at this temperature becomes significantly flattened, indicating extensive pore closure and densification driven by intense partial melting. The pore system is no longer dominated by interconnected macropores, but by isolated or poorly connected residual voids trapped within a dense matrix. This microstructural state explains the very high compressive strength values measured (above 20 MPa, Fig. 6), although these are accompanied by shape deformation due to softening (Fig. 5), which limits the strict applicability of spherical strength assumptions.

3.3. Thermal dimensional stability

Dilatometry analysis was performed using prism samples. To interpret the dimensional stability of the AAM and the realistic aggregate mix of the granulation efficiency-normalized samples, the effective alkali content per precursor mass was calculated (Table 4). Although the mass of the liquid Na_2SiO_3 activator remained unchanged during normalization, the reduced precursor mass in the pelletization efficiency normalized mixes (78 g for BA1 and 75 g for BA2) resulted in a higher specific alkali content per gram of the ash precursor. The increase in effective alkali dosage in alkali-activated samples and aggregates is relevant to the thermal behavior of the material. The thermal performance of AAM is extensively investigated for durability aspects such as thermal stress and fire resistance, where it was demonstrated that sodium-based AAMs shrink at lower temperatures compared to potassium-based ones [46]. This trend is consistent with the fact that Na^+ acts as a more effective network modifier than K^+ in silicate and aluminosilicate glasses, generally lowering glass-transition and melting temperatures and reducing melt viscosity at a given temperature [60].

The linear shrinkage behavior of the non-normalized and efficiency-normalized mixes during heating is shown in Fig. 8. The measurement results represent an approximation of thermal dimensional stability, since dilatometry was conducted on prismatic specimens instead of individual aggregates due to experimental limitations. Differences in specimen geometry and microstructure may influence heat transfer and reaction kinetics during thermal treatment, thereby affecting the observed dimensional changes. The thermal strain (dL/L_0), i.e. the relative change in sample length, and its rate, i.e. the first derivative of thermal change, reveal several distinct stages of dimensional change associated with dehydration, decarbonation, and the onset of sintering. All samples exhibit initial shrinkage below 250 °C, corresponding to the loss of physically bound water and the dehydration of the alkali-activated gel. The samples with a higher Na_2O/precursor weight ratio also exhibited a more pronounced shrinkage in this initial temperature range, likley corresponding to extent of AAM gel formation and indicating that during initial alkali activation, sufficient alkali dosing allows a better dissolution of reactive Ca–Si–Al phases and favours precipitation of the aluminosilicate network structure. The intensity of shrinkage and strain rate is most noticeable with BA1 n. (highest alkali dose per precursor), for BA1 and BA2 n. it is similar (similar alkali dose), and lowest with BA2.

A second shrinkage step occurs between approximately 500 and 800 °C, which can be attributed to dehydroxylation and partial decarbonation of Ca-bearing phases [61,62]. This stage coincides with increased open porosity and decreased bulk density observed in the MIP analysis (Table 2), caused by gas release. As the BA2 mix variants contain a lower alkali/precursor ratio compared to BA1 mixes variants, their geopolymerisation should be less extensive, leaving a larger portion of the precursor (particularly the reactive amorphous Ca-rich phases and non-reactive crystalline carbonates) remained unreacted or only partially bound in the alkali-activated matrix after curing. In addition, the lower Si/Al ratio of BA2 (approx. 1.6), which deviates from the theoretically optimal value for well-developed aluminosilicate network formation (approx. 1.9), further limited gel polymerization and reduced C–A–S–H formation, favouring instead the precipitation of hydroxides. Thereafter, upon heating, these unreacted Ca-containing phases, primarily carbonates and simple hydroxides, undergo dehydroxylation and decarbonation, releasing H_2O and CO_2 gases [63]. The temperature interval between 200 and 600 °C also overlaps with the oxidation of unburnt carbon commonly present in biomass ashes, contributing further to gas evolution and pore development [64].

The final thermal shrinkage event, observed above approximately 1000 °C, marks the onset of partial melting. The efficiency-normalized BA1 n. sample with the highest alkali content exhibited a slightly earlier onset of shrinkage and a more pronounced strain rate compared with the other mixtures. This behavior indicates that sodium from the alkaline activator acts as an effective flux at elevated temperatures [60], lowering the softening point and enhancing viscous flow due to melting. Sodium-rich silicate glasses exhibit strong melting-point depression, where addition of Na_2O act as a flux, resulting in melt formation at lower temperatures. Binary phase-diagram data show a strong decrease of the melting point in SiO_2–Na_2O systems, with eutectic liquidus temperatures falling from 1728 °C for pure silica to 840-1100 °C in Na-silicate compositions [65,66].

Table 4
Total solid alkali content (expressed as Na_2O) in original and granulation efficiency-normalized mixes. Mix variants with *n.* annotations are normalized to the pellezitazion efficiency.

Mix variant	Precursor [g]	Na_2SiO_3 activator [g]	Na_2O in activator [g]	Na_2O/precursor [wt%]
BA1	100	44.8	7.57	7.57
BA1 *n.*	78	44.8	7.57	9.71
BA2	100	32.2	5.44	5.44
BA2 *n.*	75	32.2	5.44	7.25

3.4. Thermal phase evolution

The mineralogical evolution of BA1 aggregates upon thermal treatment is shown in Fig. 9, while the corresponding refined quantitative XRD patterns, and reference codes with chemical formulas of the identified phases are provided in Fig. S2 and Table S2 in the Supplementary data. The thermally untreated aggregates exhibited a predominantly amorphous AAM matrix (over 66 wt%), with major crystalline phases including calcite (Cc), quartz (Qz), and hematite (Hm), inherited from the raw BA precursor. The high amorphous content reflects the presence of alkali-activated aluminosilicate gel phases, such as C–A–S–H type

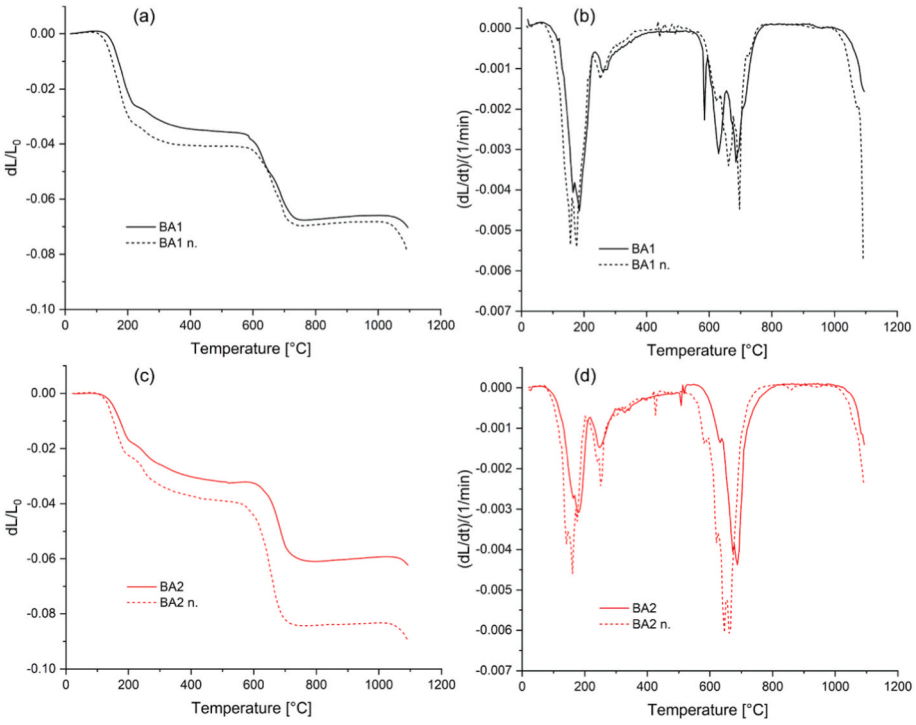

Fig. 8. Dilatometric curves of alkali-activated mixes and their granulation efficiency–normalized counterparts. (a) Thermal strain and (b) strain rate for BA1, (c) thermal strain and (d) strain rate for BA2.

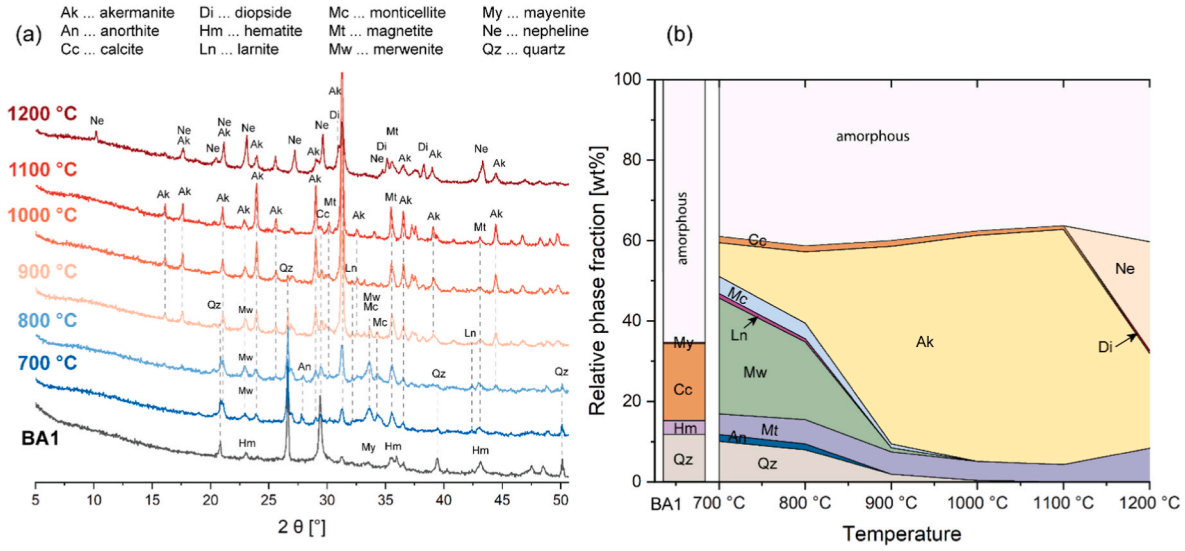

Fig. 9. Phase evolution of BA1 aggregates during thermal treatment derived from XRD analysis.

networks, which form the principal binding matrix in the aggregate.

Upon exposure to elevated temperatures, significant changes in phase composition were observed (Fig. 9). Hidayu Jamil et al. [67,68] observed that the chemical composition of the source material influences the phase transformation of the sintered geopolymers made from slag and kaolin, resulting in the formation of amorphous and crystalline phases. At 700 °C, the amorphous fraction gradually decreased, accompanied by the decomposition of calcite (Cc, $CaCO_3$) and the appearance of Ca–Mg–Si-bearing silicate crystalline phases, primarily akermanite (Ak, $Al_{0.5}Ca_2Mg_{0.75}O_7Si_{1.75}$), merwinite (Mw, $Ca_3Mg(SiO_4)_2$), larnite (Ln, Ca_2SiO_4) and monticellite (Mc, $CaMgSiO_4$). These phases are products of thermal transformation in Ca–Mg–Al–Si systems and indicate devitrification of the amorphous AAM matrix and reorganization of the gel network. The formation of melilite-group phases (akermanite and merwinite) reflects the incorporation of Mg and Si from the amorphous gel and unreacted ash particles into thermally stable crystalline frameworks.

At temperatures above 900 °C, the Ca–Mg silicate phases became dominant, with akermanite comprising the largest crystalline fraction. Keppert et al. [69] reported that thermally induced alteration of slag activated with alkaline silicate solution promotes the crystallization of new phases above 800 °C, including akermanite, which contributes to compressive strength development. However, crystallization from the amorphous phase may also induce volumetric contraction associated with structural reorganization. In alkali-activated FA-slag blends akermanite and gehlenite crystalline phases formed around 700 °C can lead

to the expansion of the pore structure from micro to macro sizes [53], where such shift in dominant pore diameters was also observed in Fig. 7. Studies on slag-based AAMs have shown that sintering and crystallization of gehlenite–akermanite ceramics can reinforce the previously thermally degraded alkali-activated matrix at temperatures above 600 °C [70]. The observed evolution of mechanical strength is governed by the combined contributions of residual amorphous phases and newly formed crystalline silicates. At intermediate temperatures (700–1000 °C), the remaining amorphous aluminosilicate matrix retains sufficient viscosity to allow viscous-flow sintering [71]. During this stage, strength development remains limited because the microstructure is still primarily controlled by a partially consolidated amorphous framework [72]. The onset of a liquid phase at these temperatures accelerates densification of aggregates. A likely reason for the increasing density is sintering in the presence of a liquid phase, resulting in a significant increase in density and strength with treatment at 1100 °C (Fig. 6, Table 3). The presence of a melt promotes particle sintering and enhanced mass transport through solution–precipitation processes, resulting in a more compact microstructure [56]. The coexistence of a liquid phase and crystallizing Ca–Mg silicates, enables densification and strengthening (Fig. 6), as the melt phase facilitates mass transport and sintering neck growth between particles [38].

Hematite (Hm, Fe_2O_3) was progressively transformed into magnetite (Mt, Fe_3O_4) as temperature increased, indicating a reducing environment in the furnace atmosphere during heating. This reduction is consistent with a semi-closed furnace atmosphere and is further enhanced by local reducing environments generated within the aggregate itself. Specifically, the decomposition and oxidation of residual carbon (Fig. 1b) from the BA release CO and CO_2 gases, which can establish a reducing atmosphere. Furthermore, localized densification and reducing conditions within the densified mass can affect this process.

At 1200 °C, a distinct transformation occurred with cystalization of nepheline (Ne, $NaAlSiO_4$) and minor amonts of diopside (Di, $CaMgSi_2O_6$). The appearance of nepheline confirms the recrystallization of Na–Al–Si–rich glassy phases, promoted by the high alkali content mainly originating from the sodium-based activator (Table 1). In addition, the partial melting of melilite-rich phases such as akermanite produces a silica-undersaturated melt, which further shifts the system into the stability field of feldspathoid (nepheline) [73]. As the silica activity decreases, the melt becomes favorable not only for nepheline crystallization but also for the limited formation of diopside as Ca–Mg–Si constituents partition into the residual melt.

The phase evolution of the BA2 aggregates with the temperature treatment followed a broadly similar trend to that observed for BA1 (Fig. 10), but with several notable differences in the relative thermal stability and formation of specific crystalline phases. At 700 °C, anorthite, which is present in BA1, was not detected in BA2. Additionally, larnite (Ln, Ca_2SiO_4) appeared in higher amount in BA2. The higher larnite content at 700 °C correlates with the more distinct shrinkage peak observed in the dilatometric curve of BA2 at this temperature, confirming a more intensive transformation of unreacted Ca-bearing phases into larnite. This behavior is consistent with the lower reactivity and reduced C–A–S–H gel formation in BA2 in alkali-activation pretreatment, due to its lower Si/Al ratio and lower alkali content, which favoured the persistence of unreacted precursor minerals and simple hydrates rather than a fully polymerized aluminosilicate matrix.

Similarly to BA1, as the temperature increased to 900 °C, the formed Ca-silicates such as larnite and monticellite progressively diminished, while akermanite became the dominant phase. However, in contrast, merwinite remained more stable at 900 °C in BA2. This difference can be attributed to the lower Na_2O/precursor ratio in BA2. Sodium acts as a fluxing agent, reducing the stability range of merwinite and promoting its earlier transformation into akermanite in BA1. A comparable fluxing effect of Na_2O has been observed in different silicate raw materials when using other sodium additives, including borax and sodium hydroxide, which enhance depolymerization of the silicate network and thus facilitate phase transformation [74]. The reduced alkali fluxing effect in BA2 due to the lower alkali activator dosage therefore delayed this transformation to higher temperatures or affected its abundance at specific temperatures. At 1200 °C, the BA2 sample showed a lower fraction of nepheline, consistent with its limited Na availability, as the sodium originates primarily from the activator and not from the precursor itself (Table 1).

3.5. TG-DTA analysis of thermal behavior

The thermal behavior of powdered BA1 and BA2, shown in Fig. 11, highlights the main thermal processes governing mass loss and phase transformations up to 1050 °C.

In the low-temperature range below 250 °C, both mixes exhibit an initial mass loss accompanied by a broad endothermic effect. This region corresponds to the evaporation of physically bound water and the release of interlayer and adsorbed water from gel-like hydration products in the AAM matrix [75,76]. The endothermic peak and 13.2% mass loss are more pronounced in BA1 (Fig. 11a), consistent with its higher

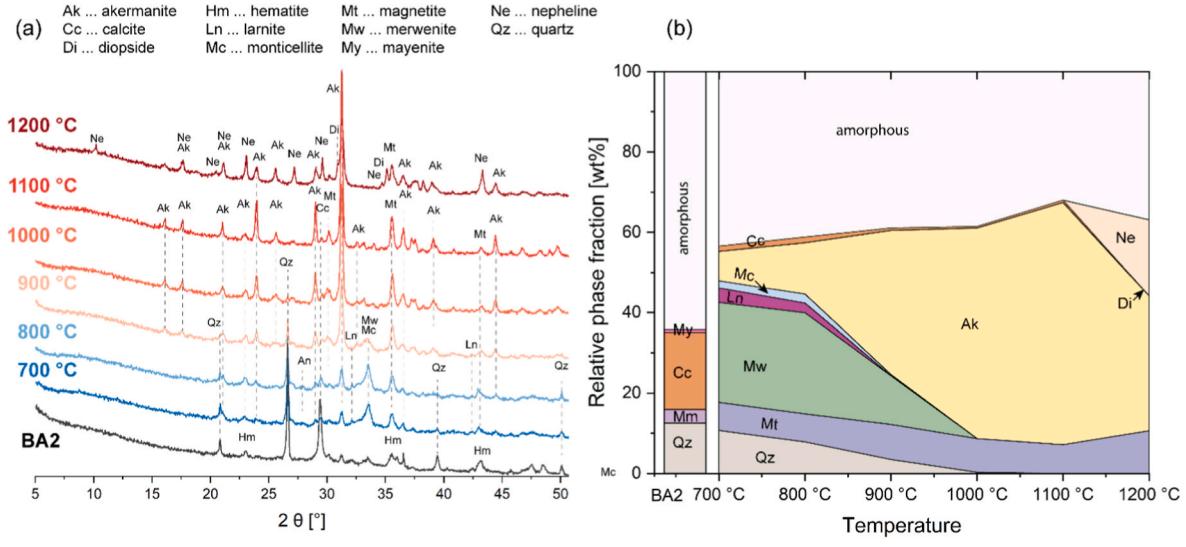

Fig. 10. Phase evolution of BA2 aggregates during thermal treatment derived from XRD analysis.

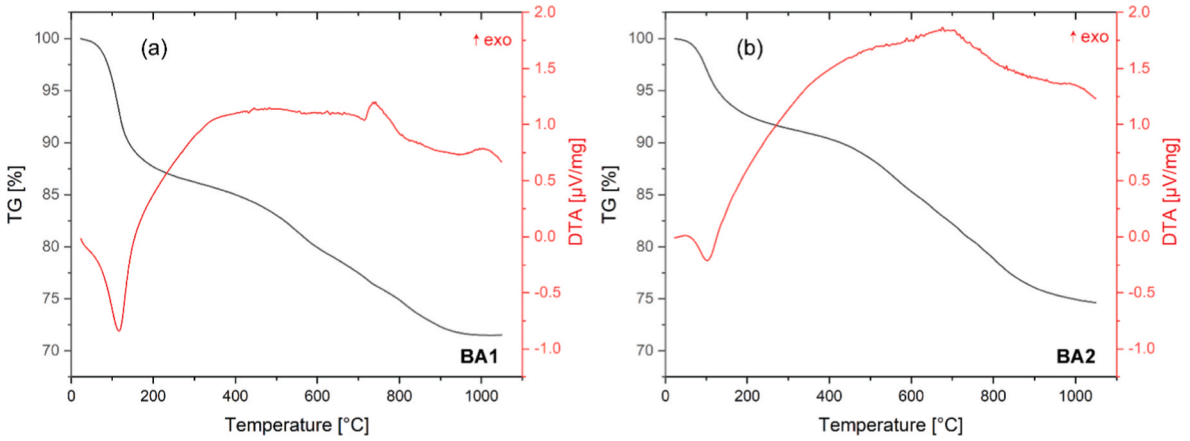

Fig. 11. Thermogravimetric (TG) and differential thermal analysis (DTA) curves of (a) BA1 and (b) BA2 powdered samples.

Na_2O/precursor ratio and, therefore, a more extensive formation of reaction products during alkali activation. This observation also aligns with the dilatometry results (Fig. 8a and b), where BA1 and BA1 n. showed greater early-stage shrinkage due to the removal of bound water from a more polymerized gel network. The TG mass loss of BA2 in this temperature range is 8.1% (Fig. 11b).

In the temperature interval between approximately 200 and 600 °C, both mixes exhibit a broad exothermic effect, associated with the oxidation of unburnt carbon commonly present in BA (Fig. 1b) [64], which becomes active as the temperature rises and oxygen availability increases within the porous matrix. This exothermic reaction indicates intrinsic heat generation within the material, originating from the combustion of residual carbon, which can locally supplement the externally supplied thermal energy during heating. Although this heat release is insufficient to induce sintering on its own, it may contribute to lowering the effective energy demand for subsequent high-temperature processes. In addition, the gradual mass losses observed in this region also reflect the onset of decarbonation of Ca-bearing phases, particularly unreacted Ca-rich components, hydroxides and carbonates [77,78].

A distinct exothermic peak at 743 °C is observed in the BA1 sample, which corresponds to the crystallization of Ca–Mg-silicate phases. High temperature crystalization thermal events were reported by De Filipps et al. [79], where DTA was used to evaluate the extent of reaction and the crystallization behavior of the anhydrous slag samples. In their study, merwinite was identified as an exothermic peak indicating nucleation before crystalizatiobn at 850 °C, while an even more intense exothermic peak at 930 °C was attributed to the crystallization of the melilite phase (reported with the general chemical formula Ca2(Mg,Al) SiO7, corresponding to the akermanite ICSD mineral card identified in our study). Similar crystalization kinetics were reported in studies of sintered bioceramics, where the main exothermic processes at 900 °C were also attributed to akermanite crystalization, supported by XRD data [80]. In contrast, our study identified this crystalization at lower temperatures due to the fluxing effects of alkali dosage. In compliance with XRD data, the exothermic peak at 743 °C corresponds to the initial stage before intense crystalization of akermanite. BA2 showed a broad, weak exothermic band from 610 to 760 °C, which aligns with the higher amount of larnite and merwinite, as less Na_2O resulted in higher thermal stability of those phases and slower akermanite crystalization. In BA2, the lower alkali dose makes the matrix less viscous, so reorganization occurs slowly over a broader temperature window. At around 1000 °C, a minor exothermic event indicates secondary crystallization or an ordering of the melilite group (akermanite, merwinite), when akermanite stabilizes as the dominant phase (Figs. 9 and 10).

3.6. FTIR

The FTIR spectra of the non-treated AAM aggregates exhibit the characteristic bands of Ca-rich alkali-activated systems (Fig. 12). The main asymmetric Si–O–T (T = Si or Al) stretching band appears at 993 cm^{-1} in BA1 and 983 cm^{-1} in BA2, indicating a subtle but significant structural difference between the two compositions. The higher wavenumber in BA1 reflects a slightly greater degree of silicate polymerization [81,82], consistent with its higher alkali content and more optimal Si/Al ratio [83], which enhance the dissolution of Si and Al species and promote the development of C–A–S–H network. In contrast, the downshift to 983 cm^{-1} in BA2 suggests a lower degree of silicate polymerization, resulting in a less condensed gel structure and lower strengths. Both spectra also show the carbonate peaks (CO_3^{2-}) of calcite at 1412, 873, and 712 cm^{-1} [84]. The bands at 796 and 776 cm^{-1} correspond to Si–O–Si symmetric stretching in quartz, while the low-frequency 466 cm^{-1} band represents the Si–O–Si bending mode typical of crystalline silicates. Minor shoulders near 512–530 cm^{-1} likely arise from Fe–O lattice vibrations or mixed Si–O–(Ca/Mg) bending in Fe- and Ca-bearing components (monticellite, larnite and merwenite) [84].

Progressive heating induces substantial changes in the vibrational spectra, reflecting the structural reorganization and crystallization observed by XRD (Figs. 9 and 10). At 700 °C, the broad Si–O–T band shifts downward to 922 cm^{-1} and becomes less defined, indicating depolymerization of the amorphous gel and the onset of Ca–Mg–Al silicate crystallization [85], observed as new peaks at 978 and 917 cm^{-1}. The carbonate bands around 873 cm^{-1} markedly decrease in intensity, confirming calcite decomposition. Si–O–Si bands at 796 or 776 cm^{-1} remain visible up to 1000 °C but begin to diminish with temperature progression, as also observed with quartz diminishing in XRD analysis [86]. A weak band near 512 cm^{-1}, visible only at 700–800 °C, corresponds to T–O lattice deformation of isolated SiO_4 tetrahedra, consistent with the formation of early Ca–Mg–Al silicates such as larnite, merwinite, and monticellite. Between 800 and 900 °C, the spectra of both BA1 and BA2 develop new peaks within the main Si–O–T region. Distinct bands at 933, 917, 853, and 978 cm^{-1}, along with new lattice modes at 704, 680, and 622 cm^{-1}, indicate the progressive crystallization of akermanite [87,88]. Above 1000 °C, the 933 cm^{-1} band becomes dominant and sharp, while the lattice deformation modes (704, 680, 622 cm^{-1}) increase in intensity, signifying the growth and structural ordering of akermanite as the principal crystalline phase [89]. At 1200 °C, both samples exhibit a marked loss of band definition across the Si–O–T region, suggesting partial vitrification. However, the 978 cm^{-1} band remains relatively pronounced, corresponding to the crystallization of melt, while the akermanite-related bands (933, 704, 680 cm^{-1}) decrease in intensity, as also observed by XRD.

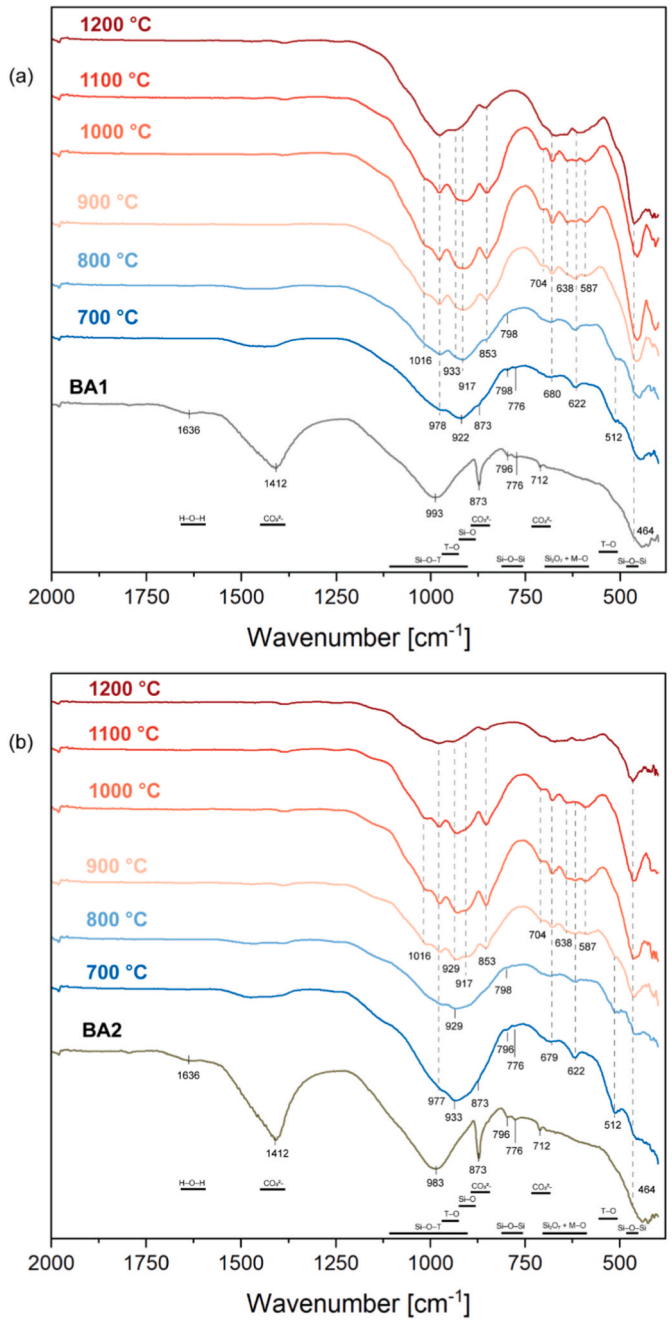

Fig. 12. FTIR spectra of alkali-activated aggregates after before and after thermal treatment: (a) BA1 and (b) BA2.

3.7. Microstructural SEM analysis

Notably, residual carbon originating from BA, observed in the raw material (Fig. 1b, and Fig. S1, Table S1 in the Supplementary data) and thermally untreated aggregates (Fig. S3 in the Supplementary material), is not observed after thermal treatment above 700 °C due to complete combustion of carbonaceous residues, which is consistent with the strong mass loss. Several studies have investigated the role of carbon admixtures in the sintering of ceramic materials, where it can impact the sintering process and microstructure. Although the primary sintering mechanisms occur between ceramic particles, carbon can contribute to a reducing atmosphere at localized sites, potentially modifying oxidation states (such as the transformation of hematite to magnetite, Figs. 9 and 10) and affecting reactions. In SiC ceramics, it was reported that carbon can modify sintering by affecting the activation energy for diffusion [68]. In ceramic materials, it was demonstrated that it can act as a pore-forming agent, burning out during thermal treatment and generating controlled porosity [67]. Increased porosity generally reduces bulk strength, but it is suitable for lightweight applications. The porosity and bulk density measurements of derived BA aggregates show that total porosity can be effectively optimized through thermal treatment. As the temperature rises above 900 °C, bulk density increases due to enhanced sintering and the onset of microstructural reorganization, indicating partial densification of the load-bearing framework while retaining a highly porous structure (Table 3). High organic residue content in BA can also be relevant to the sintering process of aggregates, as it has been demonstrated that high-carbon ashes can act as an internal partial fuel substitute during the firing period, potentially reducing the external energy required for the sintering stage and decreasing the sintering period [90]. In contrast, artificial sintered aggregates produced from conventional FA typically contain significantly lower residual carbon content, with microstructural development mainly governed by sintering and vitrification rather than pore formation. Consequently, the absence of carbon in FA limits the extent to which porosity can be tailored through burnout mechanisms.

SEM micrographs of the BA1 aggregates thermally treated at 1000, 1100, and 1200 °C, where significant compressive strength gains were observed., are shown in Fig. 13. After thermal treatment at 1000 °C (Fig. 13a and b), the microstructure shows signs of viscous particle bonding and early sintering, consistent with the gradual increase in bulk density and the slight decrease in open porosity measured by MIP (Table 3). The pore morphology changes from elongated to more rounded, and the finest pores begin to coalesce into larger voids, corresponding to the rightward shift of the dominant pore-size peak and reduced peak amplitude in the MIP pore size distribution graph (Fig. 7). This pore coalescence is characteristic of early-stage sintering, where surface energy minimization drives the merging of smaller pores into coarser ones [47,73].

With further increase in treatment temperature to 1100 °C (Fig. 13c and d), the effect becomes more pronounced, with pore walls becoming smoother and the sintered matrix more densified. These features correspond to a significant increase in bulk density and a reduction in open porosity (Table 3), as well as the initial sharp rise in compressive strength (Fig. 6). The densification behavior mirrors the major shrinkage step detected in dilatometry, where the onset of sintering-induced consolidation occurs above 1000 °C (Fig. 7).

At 1200 °C, the microstructure transforms into a partially molten, highly densified partially molten matrix with isolated spherical pores (Fig. 13e and f). Well-developed crystals with a characteristic prismatic crystallographic habit are observed within the partially molten matrix under 500 × magnification (Fig. 13f). In addition to morphology and XRD data, this was confirmed by EDXS spot analyses (Fig. S4 and Table S3 in the Supplementary data), which show Na–Al–Si compositions matching the $NaAlSiO_4$ stoichiometric field.

3.8. Role of Na_2O content in aggregation and sintering

The combined observations from mechanical behavior, dilatometry, porosity evolution, and mineralogical analysis demonstrate that Na_2O content introduced through alkali-activation pre-treatment influences sintering kinetics, phase evolution, and the final mechanical performance of the aggregates. Na_2O, primarily from the sodium silicate activator, acts as a network modifier within the aluminosilicate system, reducing melt viscosity and lowering the temperature required for viscous flow sintering. Consequently, aggregates with higher Na_2O content (BA1) show an earlier onset of shrinkage above 1000 °C in dilatometric measurements (Fig. 8), accelerated densification indicated by increased bulk density and reduced porosity (Table 3, Fig. 7), and a faster transformation of the amorphous alkali-activated matrix into thermally stable Ca–Mg silicate phases, particularly akermanite (Figs. 9

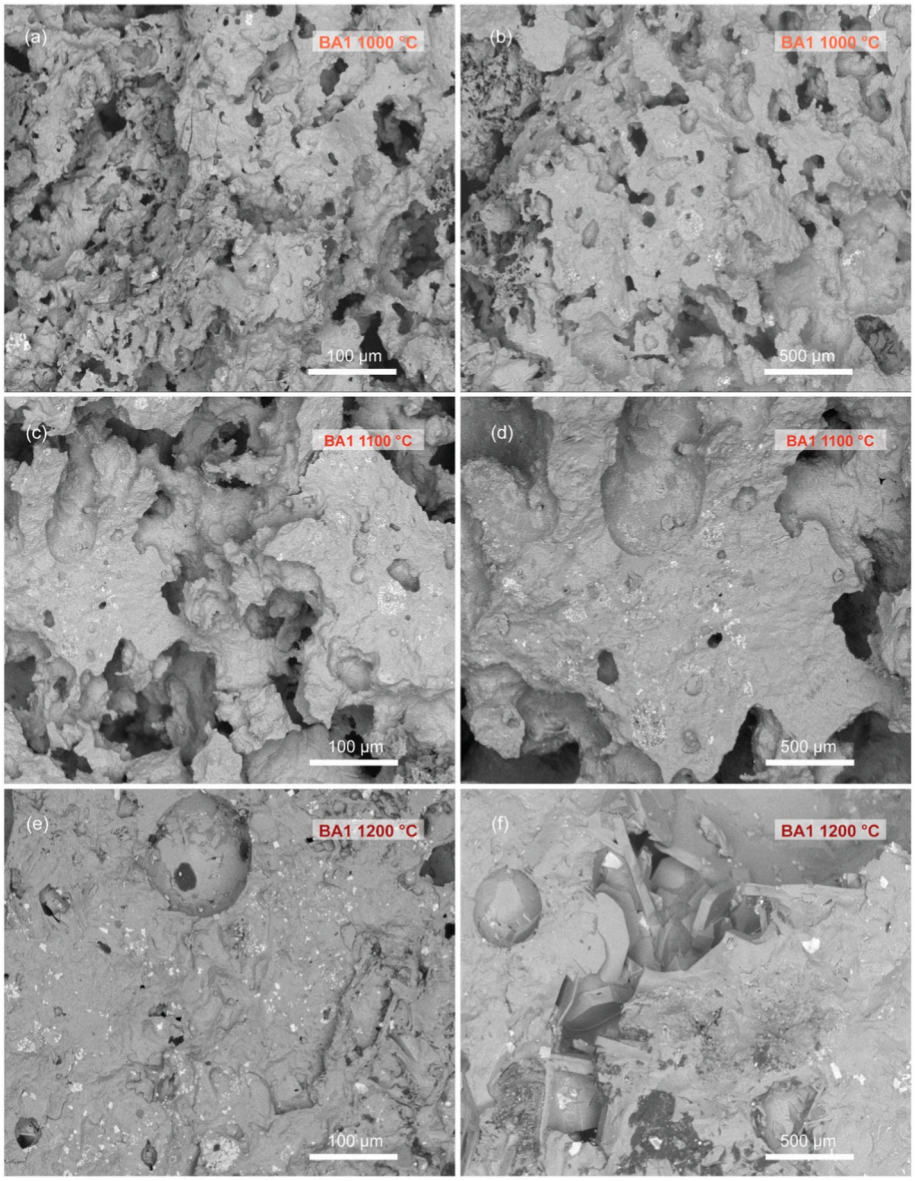

Fig. 13. SEM micrographs of BA1 aggregates after thermal treatment, shown at 250 × (right column) and 500 × (left column) magnification.

and 10). The presence of a liquid phase enhances mass transport through solution–precipitation mechanisms, promoting particle bonding and pore coalescence, which directly corresponds to the significant increase in compressive strength above 1000 °C (Fig. 6). In contrast, reduced Na_2O availability delays liquid-phase formation, stabilizes intermediate crystalline phases, and results in slower sintering kinetics and limited strength gain, as observed for BA2 across the same temperature range.

From a processing and applicability perspective, this behavior highlights alkali activation as a chemical pre-conditioning step that can modify the sintering pathway compared to conventional ceramic aggregate production. Higher granulation efficiency and stabilization of powdered BA in the initial stage before heat treatment enable a more efficient process with less unbound particles during mechanical processing [12], resulting in less waste and more efficient handling. Rather than relying solely on high-temperature firing to initiate sintering, the pre-treatment introduces alkali fluxes directly as the initial binder in the microstructure. This hybrid chemical–thermal manufacturing concept for lightweight aggregates may allow shorter firing durations or lower effective sintering temperatures, offering potential economic benefits in industrial production. Beyond lightweight aggregates, alkali-activation-assisted sintering may also be applied to other waste-derived ceramic and glass-ceramic materials, including porous insulation products, foamed ceramics, filtration media, and structural lightweight components.

4. Conclusions

Alkali-activation pre-treatment was demonstrated as an effective hybrid chemical–thermal method for producing sintered artificial aggregates from co-incineration biomass ash. The addition of sodium silicate improved granulation, enabled initial aluminosilicate gel formation, and introduced Na_2O, which acts as a flux governing sintering behavior during thermal treatment.

The results show that Na_2O availability is the key parameter controlling densification kinetics and mechanical performance. Aggregates with higher alkali content (BA1, 7.57 wt% Na_2O) exhibited earlier shrinkage onset, accelerated phase transformation towards akermanite-dominated compositions, and significantly enhanced strength development compared to the lower-alkali mix (BA2, 5.44 wt% Na_2O). The compressive strength of BA1 increased from 1.08 MPa in untreated

aggregates to 4.53 MPa at 1100 °C, reaching approximately 20 MPa after treatment at 1200 °C, accompanied by densification from highly porous structures (78% porosity) to partially vitrified matrices (34% porosity).

These findings demonstrate that alkali-activation pre-treatment enables controlled tuning of aggregate properties through thermal processing, allowing production of either lightweight porous aggregates (900–1100 °C) or dense glass-ceramic materials at higher temperatures. The study establishes co-incineration biomass ash as a viable alternative precursor to coal fly ash and identifies alkali-activation-assisted sintering as a scalable circular pathway for converting high-carbon ash into value-added construction aggregates.

CRediT authorship contribution statement

Anže Tesovnik: Writing – original draft, Methodology, Investigation, Formal analysis, Data curation, Conceptualization. **Vilma Ducman:** Writing – review & editing, Validation, Supervision, Resources, Project administration, Funding acquisition, Formal analysis, Conceptualization.

Data availability statement

The complete raw measurement data in this study is openly accessible in the DiRROS repository: http://hdl.handle.net/20.500.12556/DiRROS-24254, and upon request to authors.

Declaration of competing interest

The authors declare that they have no known competing financial interests or personal relationships that could have appeared to influence the work reported in this paper.

Acknowledgements

This research was funded by Horizon Europe ASHCYCLE project (grant number 101058162). Anže Tesovnik is supported by the Young Researcher Program within the ARIS Program Group P2-0273. The authors would also like to thank Katja Turk from the Slovenian National Building and Civil Engineering Institute for performing the DTA measurements.

Appendix A. Supplementary data

Supplementary data to this article can be found online at https://doi.org/10.1016/j.ceramint.2026.03.041.

References

[1] Directive - 2018/851 - EN - Eur-Lex, n.d. https://eur-lex.europa.eu/eli/dir/2018/851/oj/eng. (Accessed 5 October 2025).
[2] Regulation - EU - 2024/3110 - EN - EUR-Lex, n.d. https://eur-lex.europa.eu/eli/reg/2024/3110/oj/eng. (Accessed 5 October 2025).
[3] Circular economy - environment - european commission, n.d. https://environment.ec.europa.eu/strategy/circular-economy_en. (Accessed 5 October 2025).
[4] W. Langer, 9 - sustainability of aggregates in construction, in: J.M. Khatib (Ed.), Sustainability of Construction Materials, second ed., Woodhead Publishing, 2016, pp. 181–207, https://doi.org/10.1016/B978-0-08-100370-1.00009-3.
[5] EN 450-1:2012 - fly ash for concrete - part 1: definition, specifications and conformity criteria, iTeh Standards n.d. https://standards.iteh.ai/catalog/standards/cen/cc9c0d2c-6d67-4290-82ea-e5e99eb8abf0/en-450-1-2012 (accessed October 5, 2025).
[6] EN 197-1:2011 - cement - part 1: composition, specifications and conformity criteria for common cements, iTeh Standards (n.d.). https://standards.iteh.ai/catalog/standards/cen/64d327b1-d5ac-45e3-8b04-fafec9e0698e/en-197-1-2011 (accessed November 11, 2024).
[7] C618 standard specification for coal fly ash and raw or calcined natural pozzolan for use in concrete, n.d.). https://store.astm.org/c0618-22.html (accessed October 5, 2025).
[8] J.L. Provis, Alkali-activated materials, Cement Concr. Res. 114 (2018) 40–48, https://doi.org/10.1016/j.cemconres.2017.02.009.
[9] G.B. Bekkeri, K.K. Shetty, G. Nayak, Producing of alkali-activated artificial aggregates by pelletization of fly ash, slag, and seashell powder, Innov. Infrastruct. Solut. 8 (2023) 258, https://doi.org/10.1007/s41062-023-01227-1.
[10] F.K. Alqahtani, K. Rashid, I. Zafar, M. Iqbal Khan, Assessment of morphological characteristics and physico-mechanical properties of geopolymer green foam lightweight aggregate formulated by microwave irradiation, J. Build. Eng. 35 (2021) 102081, https://doi.org/10.1016/j.jobe.2020.102081.
[11] M. Balapour, W. Zhao, E.J. Garboczi, N.Y. Oo, S. Spatari, Y.G. Hsuan, P. Billen, Y. Farnam, Potential use of lightweight aggregate (LWA) produced from bottom coal ash for internal curing of concrete systems, Cement Concr. Compos. 105 (2020) 103428, https://doi.org/10.1016/j.cemconcomp.2019.103428.
[12] A. Tesovnik, L.M. Ottosen, V. Ducman, Carbonation of lightweight alkali-activated aggregates based on biomass fly ash: effect on microstructure and leaching behavior, Case Stud. Constr. Mater. 23 (2025) e05014, https://doi.org/10.1016/j.cscm.2025.e05014.
[13] T.A. Hussein, M.H. Dheyaaldin, M.A. Mosaberpanah, Y.M.S. Ahmed, H. A. Mohammed, R.R. Omer, S.M. Hamid, R. Alzeebaree, Chemical resistance of alkali-activated mortar with nano silica and polypropylene fiber, Constr. Build. Mater. 363 (2023) 129847, https://doi.org/10.1016/j.conbuildmat.2022.129847.
[14] Z. Duan, W. Yang, S. Zou, H. Liu, W. Zhao, W. Chen, A critical review on cold-bonded artificial aggregate developed from solid wastes: from granulation analysis to performance evaluation, J. Build. Eng. 99 (2025) 111588, https://doi.org/10.1016/j.jobe.2024.111588.
[15] J. Seo, S.J. Bae, D.I. Jang, S. Park, B. Yang, H.K. Lee, Thermal behavior of alkali-activated fly ash/slag with the addition of an aerogel as an aggregate replacement, Cement Concr. Compos. 106 (2020) 103462, https://doi.org/10.1016/j.cemconcomp.2019.103462.
[16] M.S. Nadesan, P. Dinakar, Structural concrete using sintered flyash lightweight aggregate: a review, Constr. Build. Mater. 154 (2017) 928–944, https://doi.org/10.1016/j.conbuildmat.2017.08.005.
[17] T. Lkhagva, E.M. Derun, N. Tuğrul, S. Pişkin, Pelletization of Fly Ashes as a Lightweight Aggregate, (n.d.).
[18] K.I. Harikrishnan, K. Ramamurthy, Influence of pelletization process on the properties of fly ash aggregates, Waste Manag. 26 (2006) 846–852, https://doi.org/10.1016/j.wasman.2005.10.012.
[19] V. Vasugi, K. Ramamurthy, Identification of admixture for pelletization and strength enhancement of sintered coal pond ash aggregate through statistically designed experiments, Mater. Des. 60 (2014) 563–575, https://doi.org/10.1016/j.matdes.2014.04.023.
[20] B. Ayati, V. Ferrándiz-Mas, D. Newport, C. Cheeseman, Use of clay in the manufacture of lightweight aggregate, Constr. Build. Mater. 162 (2018) 124–131, https://doi.org/10.1016/j.conbuildmat.2017.12.018.
[21] P.C. Lau, D.C.L. Teo, M.A. Mannan, Characteristics of lightweight aggregate produced from lime-treated sewage sludge and palm oil fuel ash, Constr. Build. Mater. 152 (2017) 558–567, https://doi.org/10.1016/j.conbuildmat.2017.07.022.
[22] Y. Huang, Z. Bian, W. Ji, M. Yio, Z. Chen, J.-X. Lu, C. Cheeseman, C.S. Poon, Production of glass-ceramic aggregates from solid wastes for high-strength and low-shrinkage lightweight mortars, Constr. Build. Mater. 416 (2024) 135244, https://doi.org/10.1016/j.conbuildmat.2024.135244.
[23] A. Ferraro, V. Ducman, F. Colangelo, L. Korat, D. Spasiano, I. Farina, Production and characterization of lightweight aggregates from municipal solid waste incineration fly-ash through single- and double-step pelletization process, J. Clean. Prod. 383 (2023) 135275, https://doi.org/10.1016/j.jclepro.2022.135275.
[24] N. Singh, J. Raza, F. Colangelo, I. Farina, Advancements in lightweight artificial aggregates: typologies, compositions, applications, and prospects for the future, Sustainability 16 (2024) 9329, https://doi.org/10.3390/su16219329.
[25] M. Collepardi, A state-of-the-art review on delayed ettringite attack on concrete, Cement Concr. Compos. 25 (2003) 401–407, https://doi.org/10.1016/S0958-9465(02)00080-X.
[26] B. Jo, S. Park, J. Park, Properties of concrete made with alkali-activated fly ash lightweight aggregate (AFLA), Cement Concr. Compos. 29 (2007) 128–135, https://doi.org/10.1016/j.cemconcomp.2006.09.004.
[27] P. Perez-Cortes, J.I. Escalante-Garcia, Gel composition and molecular structure of alkali-activated metakaolin-limestone cements, Cement Concr. Res. 137 (2020) 106211, https://doi.org/10.1016/j.cemconres.2020.106211.
[28] I.N.A. Al-Duais, S. Ahmad, M.M. Al-Osta, M. Maslehuddin, T.A. Saleh, S.U. Al-Dulaijan, Optimization of alkali-activated binders using natural minerals and industrial waste materials as precursor materials, J. Build. Eng. 69 (2023) 106230, https://doi.org/10.1016/j.jobe.2023.106230.
[29] M. Hanifa, U. Sharma, P.C. Thapliyal, L.P. Singh, Study on C-A-S-H to N-A-S-H gel conversion in fly ash-based alkali activated aggregates via accelerated carbonation: enhancing performance and inhibiting efflorescence, Journal of Sustainable Cement-Based Materials 14 (2025) 178–197, https://doi.org/10.1080/21650373.2024.2431512.
[30] L.-P. Qian, L.-Y. Xu, Y. Alrefaei, T. Wang, T. Ishida, J.-G. Dai, Artificial alkali-activated aggregates developed from wastes and by-products: a state-of-the-art review, Resour. Conserv. Recycl. 177 (2022) 105971, https://doi.org/10.1016/j.resconrec.2021.105971.
[31] R. Razak, A. Mustafa, M.M.A.B. Abdullah, H. Kamarudin, K. Nizar, D. Hardjito, Z. Yahya, Evaluation of pelletized artificial geopolymer aggregate manufactured from volcano ash, Aust. J. Basic Appl. Sci. 7 (2013) 15–20.
[32] A. Abdullah, A.M.M.A. Bakri, H. Kamarudin, C.M. Ruzaidi, Y. Zarina, M.A.A. M. Salleh, N. Zakaria, M.T.M. Faheem, Compressive strength and morphology of fly ash based geopolymer as artificial aggregate with different curing temperature, Key Eng. Mater. 594–595 (2014) 151–155. https://dx.doi.org/10.4028/www.scientific.net/KEM.594-595.151.

[33] A. Terzić, L. Pezo, V. Mitić, Z. Radojević, Artificial fly ash based aggregates properties influence on lightweight concrete performances, Ceram. Int. 41 (2015) 2714–2726, https://doi.org/10.1016/j.ceramint.2014.10.086.
[34] R.A. Razak, M.M.A.B. Abdullah, K. Hussin, K.N. Ismail, D. Hardjito, Z. Yahya, Optimization of NaOH molarity, LUSI mud/alkaline activator, and Na2SiO3/NaOH ratio to produce lightweight aggregate-based geopolymer, Int. J. Mol. Sci. 16 (2015) 11629–11647, https://doi.org/10.3390/ijms160511629.
[35] P. Gomathi, A. Sivakumar, Accelerated curing effects on the mechanical performance of cold bonded and sintered fly ash aggregate concrete, Constr. Build. Mater. 77 (2015) 276–287, https://doi.org/10.1016/j.conbuildmat.2014.12.108.
[36] A. Abdullah, M.M.A.B. Abdullah, K. Hussin, M.F.M. Tahir, Effect of different sintering temperature on fly ash based geopolymer artificial aggregate, AIP Conf. Proc. 1835 (2017) 020050, https://doi.org/10.1063/1.4981872.
[37] P. Risdanareni, J.J. Ekaputri, I. Maulidiyawati, P. Puspitasari, Mechanical properties of concrete composed of sintered fly ash lightweight aggregate, MATEC Web Conf. 195 (2018) 01008, https://doi.org/10.1051/matecconf/201819501008.
[38] M. Hujova, P.R. Monich, J. Sedlacek, M. Hnatko, J. Kraxner, D. Galusek, E. Bernardo, Glass-ceramic foams from alkali-activated vitrified bottom ash and waste glasses, Appl. Sci. 10 (2020), https://doi.org/10.3390/app10165714.
[39] P. Duxson, S.W. Mallicoat, G.C. Lukey, W.M. Kriven, J.S.J. van Deventer, The effect of alkali and Si/Al ratio on the development of mechanical properties of metakaolin-based geopolymers, Colloids Surf. A Physicochem. Eng. Asp. 292 (2007) 8–20, https://doi.org/10.1016/j.colsurfa.2006.05.044.
[40] T. Wu, S. Tang, Y.-R. Dong, J.-H. Luo, A review of the thermal and mechanical characteristics of alkali-activated composites at elevated temperatures, Buildings 15 (2025) 738, https://doi.org/10.3390/buildings15050738.
[41] A. Tesovnik, O. Lisbeth M., V. Ducman, Alkali-activated artificial aggregates. https://dirros.openscience.si/IzpisGradiva.php?id=22660, 2025. (Accessed 19 January 2026).
[42] S. Chithiraputhiran, N. Neithalath, Isothermal reaction kinetics and temperature dependence of alkali activation of slag, fly ash and their blends, Constr. Build. Mater. 45 (2013) 233–242, https://doi.org/10.1016/j.conbuildmat.2013.03.061.
[43] Z. Hu, M. Wyrzykowski, P. Lura, Estimation of reaction kinetics of geopolymers at early ages, Cement Concr. Res. 129 (2020) 105971, https://doi.org/10.1016/j.cemconres.2020.105971.
[44] S. Aldawsari, R. Kampmann, J. Harnisch, C. Rohde, S. Aldawsari, R. Kampmann, J. Harnisch, C. Rohde, Setting time, microstructure, and durability properties of low calcium fly ash/slag geopolymer: a review, Materials 15 (2022), https://doi.org/10.3390/ma15030876.
[45] F. Ameri, P. Shoaei, S.A. Zareei, B. Behforouz, Geopolymers vs. alkali-activated materials (AAMs): a comparative study on durability, microstructure, and resistance to elevated temperatures of lightweight mortars, Constr. Build. Mater. 222 (2019) 49–63, https://doi.org/10.1016/j.conbuildmat.2019.06.079.
[46] K. Traven, M. Češnovar, S.D. Škapin, V. Ducman, High temperature resistant fly-ash and metakaolin-based alkali-activated foams, Ceram. Int. 47 (2021) 25105–25120, https://doi.org/10.1016/j.ceramint.2021.05.241.
[47] P. Praneedpolkrang, N. Chaiwasee, P. Koedmontree, A. Suthiwong, H. Kaur, C. Jaturapitakkul, W. Tangchirapat, Effects of elevated temperature on mechanical properties and microstructures of alkali-activated mortar made from low calcium fly ash-calcium carbide residue mixture, Case Stud. Constr. Mater. 21 (2024) e03520, https://doi.org/10.1016/j.cscm.2024.e03520.
[48] F.B. Feldthus, L.M. Ottosen, I.M.G. Bertelsen, G.M. Kirkelund, Fluxing properties of sewage sludge ash in brick manufacturing: effect of phosphorus extraction and brick clay composition, Case Stud. Constr. Mater. 23 (2025) e05387, https://doi.org/10.1016/j.cscm.2025.e05387.
[49] G.R. Xu, J.L. Zou, G.B. Li, Effect of sintering temperature on the characteristics of sludge ceramsite, J. Hazard Mater. 150 (2008) 394–400, https://doi.org/10.1016/j.jhazmat.2007.04.121.
[50] L. Kriskova, V. Ducman, M. Loncnar, A. Tesovnik, G. Žibret, D. Skentzou, C. Georgopoulos, Alkali-activated mineral residues in construction: case studies on bauxite residue and steel slag pavement tiles, Materials 18 (2025) 257, https://doi.org/10.3390/ma18020257.
[51] M. Milat, S. Juradin, N. Ostojić-Škomrlj, A. Tesovnik, Recycling mineral wool waste: towards sustainable construction materials, Recycling 10 (2025) 174, https://doi.org/10.3390/recycling10050174.
[52] B. Horvat, A. Tesovnik, B. Mušič, Late-microwave irradiation of alkali-activated waste glass wool: linking dehydration rate with thermomechanical behaviour, in: 7th International Conference on Technologies & Business Models for Circular Economy, University of Maribor Press, 2025, pp. 11–26, https://doi.org/10.18690/um.fkkt.1.2025.2.
[53] N.K. Lee, K.T. Koh, G.H. An, G.S. Ryu, Influence of binder composition on the gel structure in alkali activated fly ash/slag pastes exposed to elevated temperatures, Ceram. Int. 43 (2017) 2471–2480, https://doi.org/10.1016/j.ceramint.2016.11.042.
[54] A. Kashani, T.D. Ngo, B. Walkley, P. Mendis, Thermal performance of calcium-rich alkali-activated materials: a microstructural and mechanical study, Constr. Build. Mater. 153 (2017) 225–237, https://doi.org/10.1016/j.conbuildmat.2017.07.119.
[55] I.H. Aziz, M.M.A.B. Abdullah, M.A.A. Mohd Salleh, S. Yoriya, J. Chaiprapa, C. Rojviriya, L.Y. Li, Microstructure and porosity evolution of alkali activated slag at various heating temperatures, J. Mater. Res. Technol. 9 (2020) 15894–15907, https://doi.org/10.1016/j.jmrt.2020.11.041.
[56] R. Shi, M. Wood, T.W. Heo, B.C. Wood, J. Ye, Towards understanding particle rigid-body motion during solid-state sintering, J. Eur. Ceram. Soc. 41 (2021) 211–231, https://doi.org/10.1016/j.jeurceramsoc.2021.09.039.
[57] W.D. Kingery, Densification during sintering in the presence of a liquid phase. I. Theory, in: S. Sōmiya, Y. Moriyoshi (Eds.), Sintering Key Papers, Springer Netherlands, Dordrecht, 1990, pp. 383–394, https://doi.org/10.1007/978-94-009-0741-6_23.
[58] P.W. Voorhees, M.E. Glicksman, Ostwald ripening during liquid phase sintering—Effect of volume fraction on coarsening kinetics, Metall Trans A 15 (1984) 1081–1088, https://doi.org/10.1007/BF02644701.
[59] R.M. German, P. Suri, S.J. Park, Review: liquid phase sintering, J. Mater. Sci. 44 (2009) 1–39, https://doi.org/10.1007/s10853-008-3008-0.
[60] M.S. Seo, I. Sohn, Substitutional effect of Na2O with K2O on the viscosity and structure of CaO-SiO2-CaF2-based mold flux systems, J. Am. Ceram. Soc. 102 (2019) 6275–6283, https://doi.org/10.1111/jace.16456.
[61] S.V. Vassilev, C.G. Vassileva, N.L. Petrova, Mineral carbonation of biomass ashes in relation to their CO2 capture and storage potential, ACS Omega 6 (2021) 14598–14611, https://doi.org/10.1021/acsomega.1c01730.
[62] M. Protić*, A. Miltojević, B. Zoraja, M. Raos, I. Krstić, Application of thermogravimetry for determination of carbon content in biomass ash as an indicator of the efficiency of the combustion process, Teh. Vjesn. 28 (2021) 1762–1768, https://doi.org/10.17559/TV-20200508110940.
[63] D.D. Burduhos Nergis, M.M.A.B. Abdullah, A.V. Sandu, P. Vizureanu, XRD and TG-DTA study of new alkali activated materials based on fly ash with sand and glass powder, Materials 13 (2020) 343, https://doi.org/10.3390/ma13020343.
[64] J. Payá, J. Monzó, M.V. Borrachero, E. Perris, F. Amahjour, Thermogravimetric methods for determining carbon content in fly ashes, Cement Concr. Res. 28 (1998) 675–686, https://doi.org/10.1016/S0008-8846(98)00030-1.
[65] B.Y. Zhakipbayev, N. Ku, Y. Zhakiyev, B.Z. Abdikadyr, Z.N. Moldamuratov, K. O. Abekov, The technology of foam-glass building materials for heat-insulating purposes using amorphous-silica rocks, ES Materials and Manufacturing 27 (March 2025) (2025) 1379.
[66] A.I. Zaitsev, N.E. Shelkova, B.M. Mogutnov, Thermodynamics of Na2O-SiO2 melts, Inorg. Mater. 36 (2000) 529–543, https://doi.org/10.1007/BF02757949.
[67] N.H. Jamil, Mohdmab Abdullah, F. Che Pa, H. Mohamad, W.M.A.W. Ibrahim, J. Chaiprapa, Influences of SiO2, Al2O3, CaO and MgO in phase transformation of sintered kaolin-ground granulated blast furnace slag geopolymer, J. Mater. Res. Technol. 9 (2020) 14922–14932, https://doi.org/10.1016/j.jmrt.2020.10.045.
[68] N.H. Jamil, M.M.A.B. Abdullah, F.C. Pa, M. Hasmaliza, W.M.A.W. Ibrahim, I.H. A. Aziz, B. Jeż, M. Nabiałek, Phase transformation of kaolin-ground granulated blast furnace slag from geopolymerization to sintering process, Magnetochemistry 7 (2021), https://doi.org/10.3390/magnetochemistry7030032.
[69] M. Keppert, D. Koňáková, K. Kulhavá, V. Pommer, J. Krejsová, E. Vejmelková, R. Černý, Thermally induced alteration of slag activated by potassium silicate, Constr. Build. Mater. 502 (2025) 144315, https://doi.org/10.1016/j.conbuildmat.2025.144315.
[70] V. Ponomar, E. Adesanya, K. Ohenoja, M. Illikainen, High-temperature performance of slag-based Fe-rich alkali-activated materials, Cement Concr. Res. 161 (2022) 106960, https://doi.org/10.1016/j.cemconres.2022.106960.
[71] T. Paul, S.P. Harimkar, Initial stage densification during spark plasma sintering of Fe-based amorphous alloy powder: analysis of viscous flow, J. Appl. Phys. 120 (2016) 134901, https://doi.org/10.1063/1.4964330.
[72] Y. Boonyongmaneerat, Mechanical properties of partially sintered materials, Mater. Sci. Eng., A 452–453 (2007) 773–780, https://doi.org/10.1016/j.msea.2006.11.043.
[73] A.K. Gupta, E.G. Lidiak, The system diopside-nepheline-leucite, Contrib. Mineral. Petrol. 41 (1973) 231–239, https://doi.org/10.1007/BF00371033.
[74] B.M. Goltsman, E.A. Yatsenko, L.A. Yatsenko, N.S. Goltsman, D.M. Kuzmenkov, Investigation of the fluxing additives effect on the foaming of different silicate raw materials, Mater. Sci. Forum 1037 (2021) 767–774. https://dx.doi.org/10.4028/www.scientific.net/MSF.1037.767.
[75] G. Zhang, K. Li, H. Shi, C. Chen, C. Yuan, Study on the effects and mechanisms of fly ash, silica fume, and metakaolin on the properties of slag–yellow river sediment-based geopolymers, Materials 18 (2025) 1845, https://doi.org/10.3390/ma18081845.
[76] F. Jin, K. Gu, A. Al-Tabbaa, Strength and drying shrinkage of reactive MgO modified alkali-activated slag paste, Constr. Build. Mater. 51 (2014) 395–404, https://doi.org/10.1016/j.conbuildmat.2013.10.081.
[77] E. Tiffo, P.D.B. Belibi, J.B.B. Mbah, A. Thamer, T.E. Pougnong, J. Baenla, A. Elimbi, Effect of various amounts of aluminium oxy-hydroxide coupled with thermal treatment on the performance of alkali-activated metakaolin and volcanic scoria, Sci. Afr. 14 (2021) e01015, https://doi.org/10.1016/j.sciaf.2021.e01015.
[78] V. Viola, M. Catauro, A. D'Amore, P. Perumal, Assessing the carbonation potential of wood ash for CO2 sequestration, Low-Carbon Mater. Green Constr. 2 (2024) 12, https://doi.org/10.1007/s44242-024-00043-9.
[79] U. De Filippis, E. Prud'homme, S. Meille, Relation between activator ratio, hydration products and mechanical properties of alkali-activated slag, Constr. Build. Mater. 266 (2021) 120940, https://doi.org/10.1016/j.conbuildmat.2020.120940.
[80] H. Mohammadi, I.Y.M. Baba, K.A. Shariff, N.A.-F. Mohd, Microstructure evolution, grain growth kinetics and mechanical properties of Ca2MgSi2O7 bioceramics sintered at various temperatures, Processing and Application of Ceramics 15 (2021) 357–365.
[81] A. Dakhane, S.B. Madavarapu, R. Marzke, N. Neithalath, Time, temperature, and cationic dependence of alkali activation of slag: insights from fourier transform infrared spectroscopy and spectral deconvolution, Appl. Spectrosc. 71 (2017) 1795–1807, https://doi.org/10.1177/0003702817704588.

[82] C.I. Merzbacher, W.B. White, The structure of alkaline earth aluminosilicate glasses as determined by vibrational spectroscopy, J. Non-Cryst. Solids 130 (1991) 18–34, https://doi.org/10.1016/0022-3093(91)90152-V.
[83] I. Ozer, S. Soyer-Uzun, Relations between the structural characteristics and compressive strength in metakaolin based geopolymers with different molar Si/Al ratios, Ceram. Int. 41 (2015) 10192–10198, https://doi.org/10.1016/j.ceramint.2015.04.125.
[84] L. Fernández-Carrasco, D. Torrens-Martín, L.M. Morales, S. Martínez-Ramírez, L. Fernández-Carrasco, D. Torrens-Martín, L.M. Morales, S. Martínez-Ramírez, Infrared spectroscopy in the analysis of building and construction materials, in: Infrared Spectroscopy - Materials Science, Engineering and Technology, IntechOpen, 2012, https://doi.org/10.5772/36186.
[85] R.K. Vempati, A. Rao, T.R. Hess, D.L. Cocke, H.V. Lauer, Fractionation and characterization of Texas lignite class 'F' fly ash by XRD, TGA, FTIR, and SFM, Cement Concr. Res. 24 (1994) 1153–1164, https://doi.org/10.1016/0008-8846(94)90039-6.
[86] Z. Zhang, H. Wang, J.L. Provis, Quantitative study of the reactivity of fly ash in geopolymerization by FTIR, Journal of Sustainable Cement-Based Materials 1 (2012) 154–166, https://doi.org/10.1080/21650373.2012.752620.
[87] R. Gören, B. Ersoy, C. Özgür, T. Alp, Colloidal stability–slip casting behavior relationship in slurry of mullite synthesized by the USP method, Ceram. Int. 38 (2012) 679–685, https://doi.org/10.1016/j.ceramint.2011.07.056.
[88] M. Criado, A. Fernández-Jiménez, A. Palomo, Alkali activation of fly ash: effect of the SiO2/Na2O ratio, Microporous Mesoporous Mater. 106 (2007) 180–191, https://doi.org/10.1016/j.micromeso.2007.02.055.
[89] J. Temuujin, K. Okada, K.J.D. MacKenzie, Effect of mechanochemical treatment on the crystallization behaviour of diphasic mullite gel, Ceram. Int. 25 (1999) 85–90, https://doi.org/10.1016/S0272-8842(98)00005-4.
[90] T.Y. Lo, H. Cui, S.A. Memon, T. Noguchi, Manufacturing of sintered lightweight aggregate using high-carbon fly ash and its effect on the mechanical properties and microstructure of concrete, J. Clean. Prod. 112 (2016) 753–762, https://doi.org/10.1016/j.jclepro.2015.07.001.